Master's Thesis, 30 ECTS

Hyperspectral Scanning for Adaptable Insect Light Scattering Model

Division of Combustion Physics
Department of Physics
Faculty of Engineering LTH
Lund University

LUND UNIVERSITY

Author:
Dorota Kizewska

Supervisor:
Meng Li
Co-supervisor:
Timotej Zuntar
Mikkel Brydegaard

June 2026

Abstract

Monitoring insect populations and diversity are important to assess ecosystem health. Traditional trapping and manual identification methods are slow and labor-intensive. Entomological lidar offers an automated alternative for monitoring insects in flight, but classifying species remains a challenge. Building empirical databases through catch-and-release methods is impractical due to the enormous number of insect species. As an alternative, this thesis focuses on laying the groundwork for a physics-based model by isolating the optical properties of the insect body. Hyperspectral reflectance data of female *Aedes aegypti* mosquitoes were acquired in the shortwave infrared region (960–2500 nm) across two orthogonal rotation axes (yaw and roll) using de-polarized backscatter signal. A four-parameter diffuse reflectance model, which accounts for water and melanin absorption along with scattering parameters, was fitted to the recorded spectra, achieving more than 98% (R^2) agreement. A MATLAB framework was then developed using spherical harmonics to parameterize the angular dependence of these optical properties. This allows the framework to output the backscatter optical cross-section (OCS) σ_{BS} as a function of pitch, yaw, and wavelength, providing foundational data for future insect lidar models.

Acknowledgements

My amazing supervisor Meng Li, co-supervisors Mikkel Brydegaard and Timotej Zuntar, David Dreyer for his invaluable biological expertise, and all members of the research group for their support, feedback and advice. Mengistu Dawit Bulo, Rickard Ignell, SLU for providing the live specimen without which this project would not have the form it has now, Nina Reistad for lending us the lab equipment, my partner Alex, who has always supported me and made it possible to pursue this degree in the first place, my classmates and friends who made the studies fun and exciting.

Contents

Abstract i

Acknowledgements ii

1 Introduction 1
- 1.1 Motivation . . . 1
- 1.2 State of the Art . . . 2
- 1.3 Aim and Scope . . . 4

2 Theory 5
- 2.1 Conceptualizing Insects as Parametrization Targets . . . 5
- 2.2 Dominant short wave infrared absorbers for insects . . . 6
- 2.3 Diffuse Reflectance . . . 8
- 2.4 Backscatter Optical Cross Section . . . 10

3 Materials and Methods 11
- 3.1 Specimen Preparation and Mounting . . . 11
- 3.2 Shortwave Infrared Hyperspectral Imaging System . . . 11
- 3.3 Data Processing and Thresholding . . . 13
- 3.4 Scan Geometry . . . 14
- 3.5 Computational OCS Framework . . . 14

4 Results and Discussion 17
- 4.1 Extraction of Optical Parameters . . . 17
- 4.2 Angular Dependence of Optical Parameters . . . 18
- 4.3 Methodological Challenges and Limitations . . . 20
  - 4.3.1 Insect and Scan Geometry . . . 20
  - 4.3.2 Image Processing and Masking . . . 20
  - 4.3.3 Environmental and Biological Variances . . . 21
- 4.4 Application of the Simulation Framework . . . 22
- 4.5 From Laboratory Specimens to Field Lidar Observation . . . 23

5 Conclusions 25

6 Outlook 26

7 Appendix. Supplementary Data 33

1 Introduction

1.1 Motivation

Insects are an abundant group of animals, with an enormous number of species. Their populations and diversity are critical indicators of ecosystem health [1], although some insects act as disease vectors of humans [2]. Monitoring these insects populations and differentiating the types of insects present is invaluable, as it provides insights needed to improve agricultural pest management, protect key pollinators and control disease vectors.

Traditional methods are often expensive, slow, and labor-intensive. A good example reflecting this issue is the *Swedish Malaise Trap Project*, which originally ran its field campaign from 2003 to 2006 [3]. After 15 years of work, out of an estimated 20 million collected specimens, they have identified about 1% so far, including over 4000 species, of which some were never recorded before [3]. This was mainly done by manual hand-sorting with the help of volunteers and traditional morphological identification by taxonomists, costing around 30 million SEK. Although a tremendous amount of data has been processed through these efforts, much more remains to be done. Furthermore, taxonomists are typically highly specialized to a single insect group, and there is a profound imbalance in expertise across different Orders. Popular groups such as Coleoptera like beetles or Lepidoptera like butterflies attract considerably more taxonomic experts than hyper diverse but unpopular groups like Diptera such as flies and parasitoid wasps [4]. This taxonomic bias creates an artificial bottleneck, as manual identification speed is strictly dictated by the lack of available specialists. The *Swedish Malaise Trap Project* report itself acknowledges that this manual sampling and identification approach is too slow [3], noting the need for modern techniques in future large-scale inventories, highlighting the demand for advanced, automated solutions. While advancements are being made on identification methods for the malaise trap catches, for example the genetic analysis approach applied by Prof. Fredrik Ronquist and his team, the ability to skip the capturing of physical insects altogether would be invaluable.

1.2 State of the Art

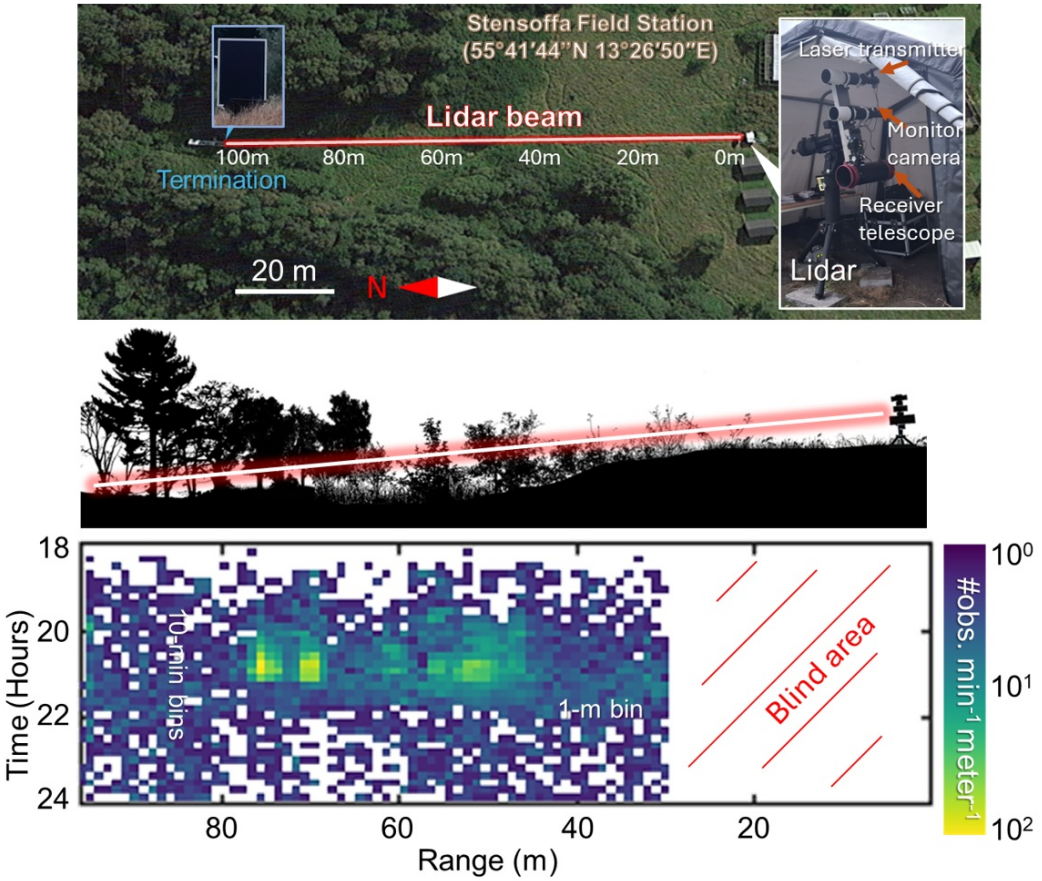

Figure 1: Overview of a typical entomological lidar system and recorded insect activity map. This figure, originally from [5], illustrates the deployment of the lidar system at Stensoffa Field Station (55°41'44"N 13°26'50"E).

Entomological lidar has emerged as a powerful tool for this purpose, capable of high-volume, non-invasive insect detection (see Figure 1). The system operates by emitting a laser beam and collecting the backscattered light, recording the precise time and location of each insect observation. By employing a Scheimpflug configuration and triangulation, the entire detection transect remains sharply in focus. This allows the lidar to monitor the entire range simultaneously, capturing clear signals for any insect passing through the beam path. The characteristics of the backscattered signal depend on the probing laser's wavelength and polarization state. By utilizing different combinations of these optical properties, existing lidar systems can extract a wealth of information, differentiating physical and behavioral traits such as wingbeat frequency, body and wing size, specularity, wing thickness, melanization, flight trajectory, heading, and speed [6, 7, 8, 9]. In general, lidar observations are grouped based on similarities within the signals themselves, which inherently reflect the physical and behavioral traits of the insects. The approach in the Biophotonic Sensing Group here at Lund University involves extracting the power spectrum of the observations and grouping them using hierarchical cluster analysis (HCA), see example showing in Figure 2. This clustering method showing a 70% correlation in cluster richness [10] at the family level when validated against side-by-side Malaise trap catches.

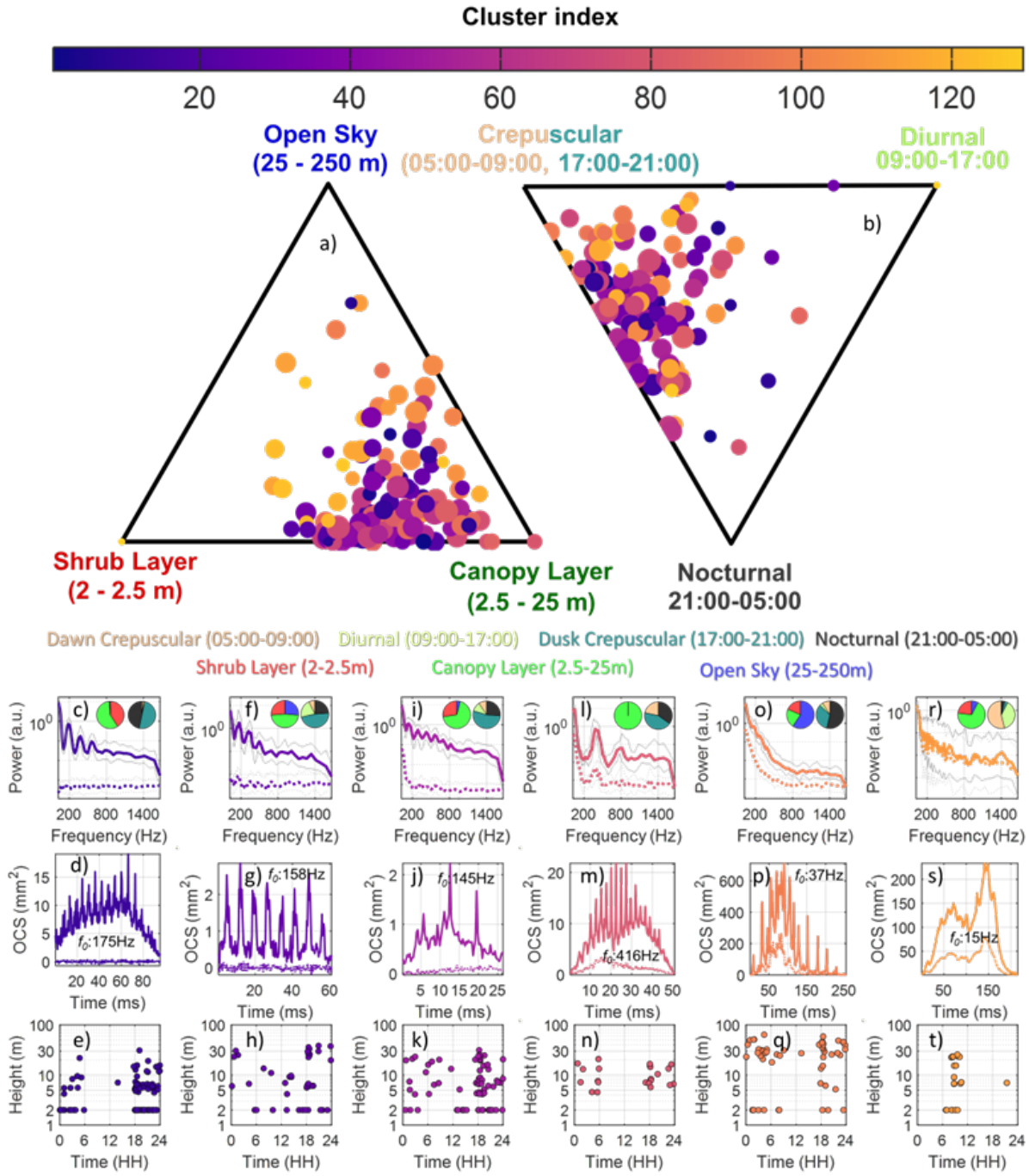

Figure 2: Example of lidar signal diversity for observations recorded from Taï National Park, Ivory Coast. This figure, originally from [7], shows data from a polarization lidar used to assess insect biodiversity along a forest edge. An unsupervised hierarchical clustering analysis grouped the signals by similarity of their frequency spectra, resulting in 129 distinct clusters which can be used to estimate species richness. The various panels demonstrate the clustering of raw waveforms and power spectra, alongside the resulting spatiotemporal distributions of specific insect groups.

While clustering lidar signals with HCA provides a valuable proxy for diversity variations, pushing beyond it to pinpoint specific functional groups, genera, or individual

species remains a challenge. Achieving this level of precision requires a comprehensive library of known signals for comparison, and such library must incorporate the influence of the insect's body and wing orientation, alongside natural variations between individuals of the same species, such as differences in size, life stage, diet (e.g. nectar or blood) or reproductive status. Logically, one might approach this by releasing known insect species into the sensor's path to build a supervised training dataset. Feeding known species features into a model for identification is a common method in AI machine vision studies [11], and within photonic sensor research, signatures have been recorded by releasing known species into controlled cages [10]. However, this empirical approach is expensive and time-consuming. Because insects represent the most diverse group of animals on Earth [12], capturing and recording every species to train a dataset is unfeasible in terms of time and realistic budget. While researchers often narrow their scope to prioritize specific insects based on their economic or ecological value, such as agricultural pests or key pollinators, this selective approach still faces practical challenges. First, training a robust model requires gathering thousands of data points for just a single species. Second, the experimental setup itself alters the data; caged insects can exhibit different flight behaviors compared to those in the open field. Finally, even if environmental conditions are controlled, natural biological variance remains a hurdle, as wingbeat frequency alone varies by at least 25% within the exact same species, sex, temperature and humidity [10]. The time and financial costs required to build an empirical database through physical measurements are not justified by the output, leaving a critical methodological gap. While all insect species are made of the same molecular bulk constituents (water (70%), chitin, melanin, lipids), their genetic blueprint differs for the structure of their body, wings, tissue and nano-surfaces. Therefore, precise micro- and nano-measures of physical structure and path lengths is key to differentiate species.

1.3 Aim and Scope

As an alternative to the impractical task of physically recording millions of species, the methodological gap could be addressed by developing an adaptable, physics-based model to simulate the lidar scattering signatures of insects. The research group aims to build such a model, covering body and wing geometry, wingbeat dynamics, and light interactions like specular reflection and polarization across all orientations. While establishing this comprehensive model is the long-term goal, this thesis focuses on laying the essential groundwork by isolating the optical properties of the main body. To achieve this, I first acquired hyperspectral reflectance data of *Aedes aegypti* across two orthogonal rotation axes in the shortwave infrared, using de-polarized backscatter. I then fitted a diffuse reflectance model, accounting for water and melanin absorption, to the recorded spectra to characterize the angular dependence of the optical parameters. Finally, I developed an adaptable MATLAB simulation framework that outputs the backscatter optical cross-section of the insect body as a function of pitch, yaw, and wavelength.

2 Theory

2.1 Conceptualizing Insects as Parametrization Targets

When light hits the insect, it is partially absorbed and partially scattered in different directions, including backscattering towards the source and forward scattering through the insect body . The first part is described by the back-scatter optical cross-section, σ_{BS}, and depends on the reflectance, R, of the surface and the projected area, A[13]. In this project, we focus on hyperspectral imaging of female *Aedes aegypti* and extracting optical parameters from de-polarized measurements using diffuse reflectance model of backscatter light.

The lidar signal can be decomposed into body and oscillatory wing part components, as shown in Figure 2 (d, g, j, m, p, s), where the general envelope trend is the body signal and the rapid oscillations are wing reflections. This body signal component primarily consists of backscattered light from the main physical mass of the insect body (head, thorax, abdomen), smaller parts like legs and antennae generally contribute minimally to the back scattered signal due to their small area.

Because entomological lidar detects insects flying freely in open space, the measured signal depends on the insect's physical orientation relative to the sensor. To accurately simulate this body signal from any viewing angle in three dimensions, it is necessary to mathematically recreate the three-dimensional geometry of the target. Insect bodies only have bilateral symmetry (i.e., left–right mirror symmetry across the sagittal plane along the anterior–posterior axis), and an elongated form, so they can be efficiently expressed using simple spherical harmonic models (see Figure 3). The complexity of the required model depends directly on the insect's morphology. For instance, an insect with complicated anatomical features, such as a bark beetle with open elytra, would require a larger set of parameters and higher-order spherical harmonics to describe its geometry [14]. In contrast, a mosquito (Diptera) body might be considered an ellipsoid shape, which is approximated using only a few low-order spherical harmonics.

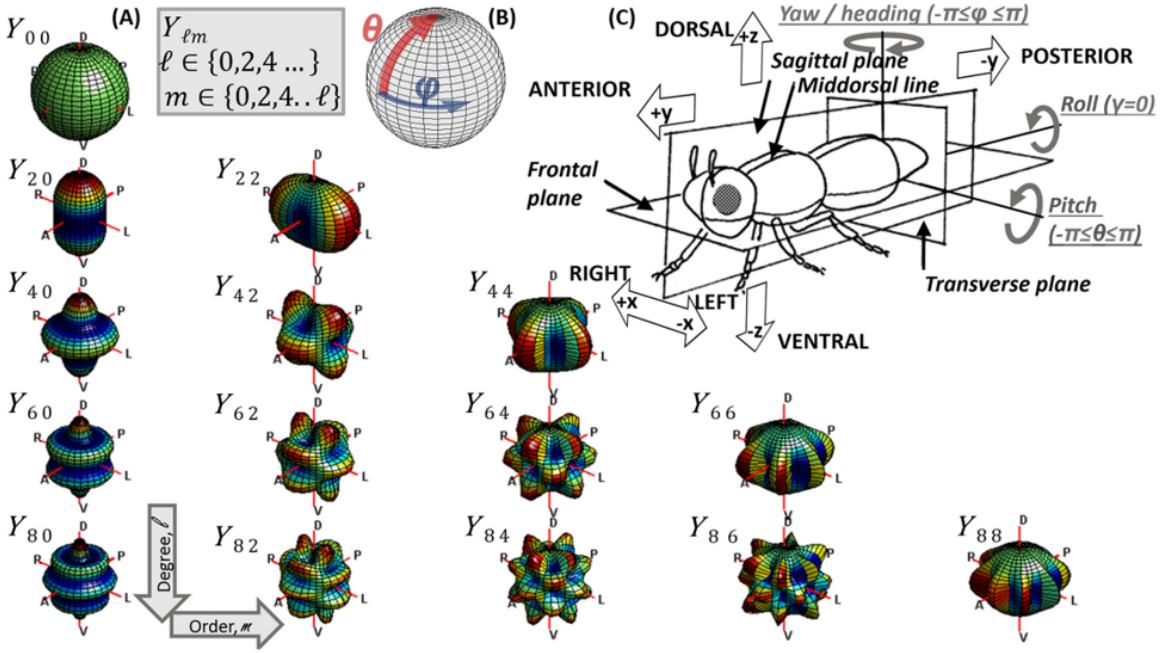

Figure 3: As a mathematical tool, spherical harmonics allow us to break down a complex shape—like an insect—into a sum of simple, well-defined shapes. As shown in this figure, originally from [15], the first few harmonics are simple (like a sphere or a dumbbell shape) and they become progressively more detailed. Once the complex scattering pattern is broken down into these components, information about the complicated 3D pattern can be stored as a simple list of coefficients.

Using Fourier techniques, any signal can be decomposed into a linear combination of periodic functions. Similarly, when considering three dimensional objects, any closed shape can be described by spherical harmonics [16]. This is helpful for modeling, as this mathematical parameterization reduces computational requirements. Both the insect geometry and optical characteristics are stored as matrices of spherical harmonic coefficients. These continuous analytical functions allow for spatial rotations, enabling the calculation of the target's projected area and optical cross-section from any viewing angle. By combining this geometry with the diffuse reflectance parameters extracted in this thesis, a reference library can therefore be constructed in future work using only these coefficients, where the 3D structure is rendered only when required.

2.2 Dominant short wave infrared absorbers for insects

When light interacts with biological tissue, it can be scattered, transmitted, or absorbed. The total absorption of the light depends on the wavelength-specific absorption coefficient of the medium and the optical path length the light travels through the tissue, following the principles of the Beer-Lambert law. In the shortwave infrared (SWIR) region investigated in this thesis (960–2500 nm), the dominant biological absorbers in a mosquito target are melanin and liquid water, with minor contributions from lipids (as shown in Figure 4). The values of water, melanin, and lipid absorption coefficients were taken from [17], [8], and [18] respectively.

As illustrated in the absorption spectra (Figure 4), melanin exhibits its strongest absorption at the shorter wavelengths of the SWIR window, and its absorption coefficient

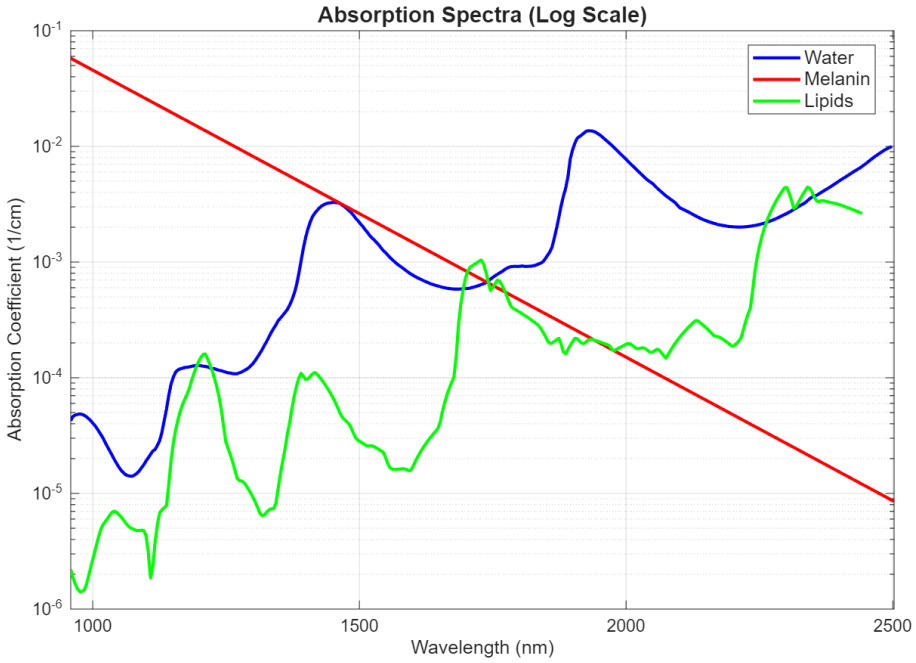

Figure 4: Absorption spectra of dominant biological absorbers in the shortwave infrared (SWIR) region. The graph displays the wavelength-dependent absorption coefficients of liquid water, melanin, and lipids.

strictly decreases exponentially as the wavelength increases. Conversely, liquid water is a highly structured absorber and the main contributor to the insect's overall weight, particularly within the abdomen and thorax. In this thesis we use a hyperspectral SWIR camera, HySpex SWIR-640. Within the camera's spectral window, water displays two distinct, strong absorption peaks at approximately 1450 nm and 1930 nm. Water characteristics have historically served as a critical factor in remote sensing; for instance, it has been used in radar cross-section measurements of insects to estimate their total body mass [19]. Additionally, variations in water content can serve as indicators of different physiological states, such as dehydration or feeding status. While a blood-fed mosquito could potentially exhibit hemoglobin absorption signatures, the mosquito specimens used in this study were exclusively fed on sugar water see Figure 5. Finally, while lipids present discernible, narrow absorption peaks (most notably around 1200 nm, 1750 nm, and 2300 nm), water remains the dominant absorber at longer wavelengths, making water and melanin the primary focus for the diffuse reflectance model for mosquito.

Figure 5: Preparation and mounting of mosquito specimens. The live mosquitoes were provided by the Swedish University of Agricultural Sciences (SLU). Mosquito were fed with sugar water instead of blood meal. The right panel illustrates a single freshly killed mosquito mounted on a pin, prepared for hyperspectral scanning.

2.3 Diffuse Reflectance

The total reflectance can be decomposed into specular surface-reflected light (R_{spec}) and light that is multiply-scattered inside the body (R_{diff}). In this thesis the main focus is on diffuse reflection. In previous works [13], the Kubelka-Munk [20] theory was used to describe it. Specifically, the model relies on Equation 44 from Kubelka's 1948 work, which was explicitly derived to describe "thin specimens of poorly scattering material." The theory takes sample thickness, and scattering and absorption mean-free-path as the factors dictating diffuse reflectance (and transmittance). The terms "scatterance" $S(\lambda)$ and "absorbance" $A(\lambda)$ are introduced to simplify the description, defining the fundamental diffuse reflectance as:

$$R_{diff}(\lambda) = \frac{S(\lambda)}{1 + S(\lambda) + A(\lambda)} \tag{1}$$

In the short-wave infrared region, the scatterance follows a simple empirical power law [21] and can be described as:

$$S(\lambda) = \left(\frac{D_{\frac{1}{2}}}{\lambda} \right)^{\alpha} \tag{2}$$

Here, $D_{1/2}$ represents the exact theoretical wavelength at which 50% of the incident light is diffusely backscattered, assuming the material contains no biological absorbers. And for α, higher values indicate Rayleigh-like scattering from smaller structures, while lower values suggest scattering from larger cellular features.

The measured reflectance is attenuated by absorption ($A(\lambda) \neq 0$). This absorbance depends on the molecular composition of the body. For mosquitoes in the near infrared

region, the most significant absorption will come from melanin and water, giving:

$$A(\lambda) = l_{H_2O}\mu_{H_2O}(\lambda) + l_{mel}\mu_{mel}(\lambda) \tag{3}$$

where l_{H_2O}, l_{mel} are the absorption path-lengths of water and melanin respectively and, μ_{H_2O}, μ_{mel} are their wavelength-dependent absorption coefficients (whose specific spectral profiles are shown in Figure 4). Together with $D_{1/2}$ and α, these path-lengths form the four free parameters $\{D_{1/2}, \alpha, l_{H_2O}, l_{mel}\}$ that are fitted to each measured spectrum throughout this thesis. A visual representation of these parameters extracted from previous single-angle hyperspectral scans is shown in Figure 6. Notably, these optical parameters can vary across the insect's body [22], although for the purpose of developing a rudimentary model of a mosquito, have been approximated as uniform.
The total wavelength-dependent reflectance of the insect body is then ([13])

$$\begin{aligned}\hat{R}_{body}(\lambda) &= R_{spec} + R_{diff} = R_{spec} + \frac{S(\lambda)}{1 + S(\lambda) + A(\lambda)} \\ &= R_{spec} + \frac{\left(\frac{D_{\frac{1}{2}}}{\lambda}\right)^{\alpha}}{1 + \left(\frac{D_{\frac{1}{2}}}{\lambda}\right)^{\alpha} + l_{H_2O}\mu_{H_2O}(\lambda) + l_{mel}\mu_{mel}(\lambda)}.\end{aligned} \tag{4}$$

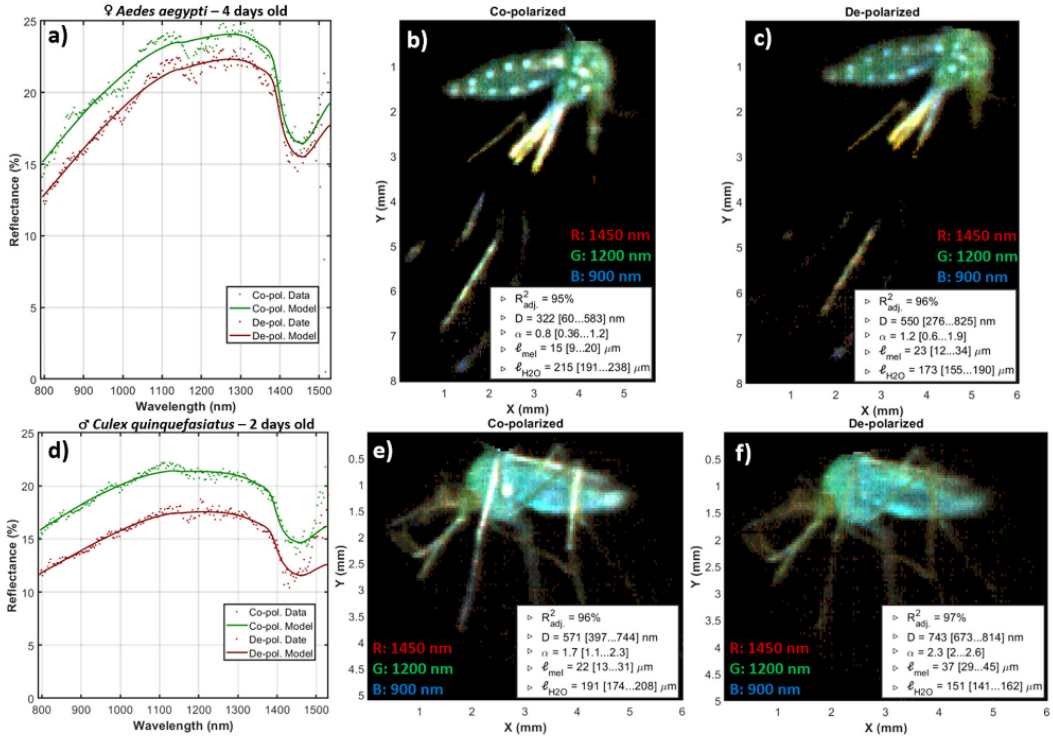

Figure 6: Mosquito hyperspectral analysis, originally from [13]. The model in this project should be able to qualitatively replicate the co-pol model in sub-figure a). Sub-figures b), c) show hyperspectral images of female *Aedes aegypti* and sub-figures e), f) of male *Culex quinquefasiatus*. The images also show the different values of scattering parameters obtained [13].

2.4 Backscatter Optical Cross Section

The goal of the model is to simulate realistic lidar signals. The signals shown in Figure 1 are measured as an optical cross-section (σ) with units of mm^2, which represents the effective area of the target that intercepts and scatters light back towards the detector. Therefore, to allow for a direct comparison between our model and the field data, our simulated results must be calculated in the same unit. The optical cross section can be described as

$$\sigma(\lambda) = A_p \cdot R_{body}(\lambda), \tag{5}$$

where A_p is the projected area of the insect in mm^2 [13], as seen by the lidar which depends on its orientation or aspect angle described by its yaw (ψ) and pitch (ϕ) angles. $R_{body}(\lambda)$ is the surface reflectance (unitless), which depends on the wavelength λ of incident light. We therefore have a set of extrinsic (λ, ψ, ϕ) and intrinsic $(D_{1/2}, \alpha, l_{H_2O}, l_{mel})$ properties.

3 Materials and Methods

3.1 Specimen Preparation and Mounting

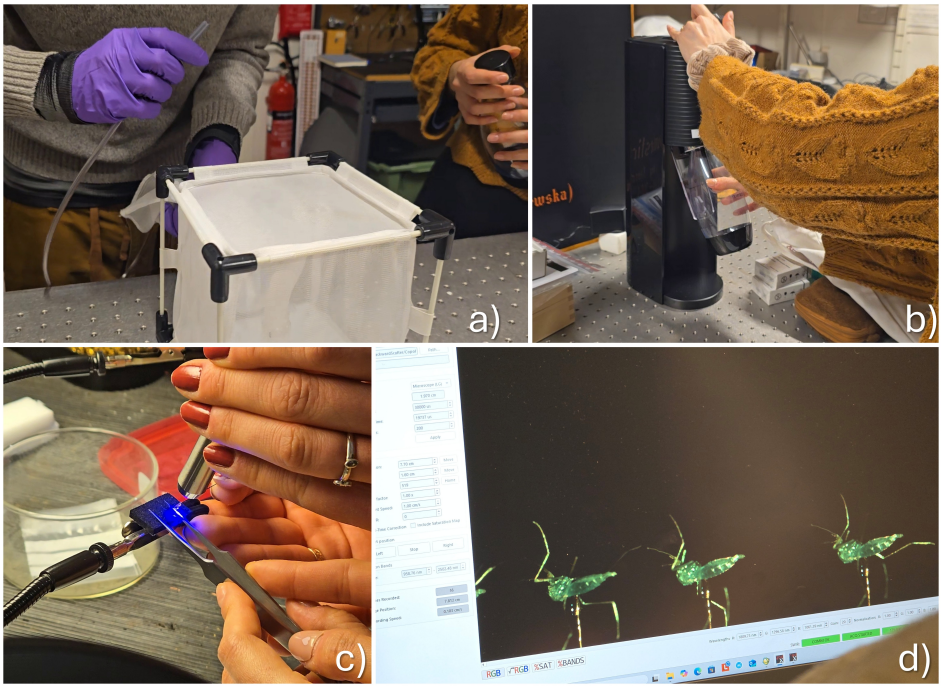

Figure 7: Overview of the specimen preparation and scanning workflow. a) Capturing individual mosquitoes from the rearing cage using a custom mouth aspirator. b) Euthanizing the specimens using carbon dioxide gas generated by a commercial carbonator. c) Carefully mounting the euthanized insects onto matte-black pins using a UV-curing adhesive. d) Live false-color preview of the mounted mosquitoes during a hyperspectral scanning session.

The mosquitoes used in this study were supplied by the Swedish University of Agricultural Sciences (SLU) in Alnarp, Sweden. While various life stages were provided, data acquisition was limited to adult females. The studied specimen were euthanized using carbon dioxide (soda stream), de-winged, and mounted on matte-black metal pins using UV glue, see Figure 7. The goal was to position the pin (and therefore rotation axis for scanning) within one of the anatomical planes of the insect and in the midpoint of body length in that plane. Such positioning allows for accurate portrayal of the symmetries of the specimen during analysis (see Figure 3) and keeps the focus of the camera uniform during scanning, respectively.

3.2 Shortwave Infrared Hyperspectral Imaging System

The hyperspectral scanning was performed using the HySpex SWIR-640 camera (Hyspex, Norsk Elektro Optikk, Norway) which operates an HgCdTe (MCT) sensor in the shortwave infrared spectral range of 960-2500 nm. The spectral and spatial resolutions are 4.3 nm, and 32 um per pixel respectively [23]. Every camera exposure captures a continuous spectrum across 362 bands, ultimately forming a full 3D hyperspectral data cube composed of two spatial dimensions and one wavelength dimension. This spectral range

was chosen to extend the 800-1500 nm range used in previous work [13], which contains one water absorption band and a significant region of melanin absorption, both of which are crucial features for species identification. The 960-2500 nm range still covers part of the melanin absorption region while adding a second, stronger water absorption band near 1930 nm. Being able to investigate two water absorption bands in the same spectrum is particularly interesting, as it tests whether a single effective water path length can self-consistently explain both bands, which themselves differ by an order of magnitude in absorption coefficient. The extended range also opens up broadband phenomena such as the spectral slope of tissue at longer wavelengths, where scattering is weaker. Importantly, the same camera and 960–2500 nm range have previously been used in our research group to study insect wing interference patterns [24], which were identified as a promising feature for remote insect identification. Working within the same spectral window therefore positions the body-scattering characterization developed in this thesis to be directly combined with that earlier wing-related work in future models.

The samples are illuminated by a tungsten filament lamp (black body radiator following a Planck curve spectrum) fitted with a wire grid linear polarizer. The light source is oriented at a 30 degree angle to the camera direction, as shown in Figure 8. The samples are mounted on the target holder, which itself is situated on a motorized translational stage with a rotating platform controlled by the Hyspex software. A linear polarizer was fixed in front of the camera objective with a 3D printed holder, which can be rotated to switch between co-polarized and de-polarized mode. Here, we understand 'co-polarized' as aligned with the polarization direction of the light source and 'de-polarized' as orthogonal to the polarization direction of the light source. Multiple scattering in biological tissue de-polarizes the light, meaning the back scattered light carries no preferred polarization; by symmetry, a linear analyzer transmits 50% of this de-polarized component regardless of its orientation. Some de-polarized signal is therefore can present in 'co-polarized' measurements, the main difference being that only the 'co-polarized' setting will accept specular signal, such as the specular reflection from the pin the insect is glued on. To minimize specular reflections and background noise, a box coated internally and externally with black neoprene foam was positioned at the far end of the camera's field of view.

The backscatter of each sample is recorded from 36 different angles in both co-polarized and de-polarized configurations. Additionally, a Lambertian gray standard reference (Spectralon®) with 50% reflectance is recorded at both polarizations for calibration purposes. To account for the instrument response and the illumination spectrum, the raw intensity of the sample must be calibrated into a reflectance value. Because the HySpex camera features an inbuilt mechanical shutter that automatically subtracts the dark current from the data file , the reflectance R for a given spatial pixel y and wavelength λ simplifies to:

$$R(y, \lambda) = \frac{I_S(y, \lambda)}{I_W(y, \lambda)} \tag{6}$$

where I_S and I_W are the raw intensity values from the sample image and the Spectralon white reference, respectively. Importantly, because the samples are calibrated against a diffuse Lambertian standard, any highly directional specular reflections from shiny features (such as insect wings or tiny legs) can exceed 100% diffuse reflectance. However, because the primary focus of this study is to isolate and analyze the multiply-scattered diffuse reflectance from the main insect body, these extreme specular reflections are treated as artifacts and excluded from the regions of interest.

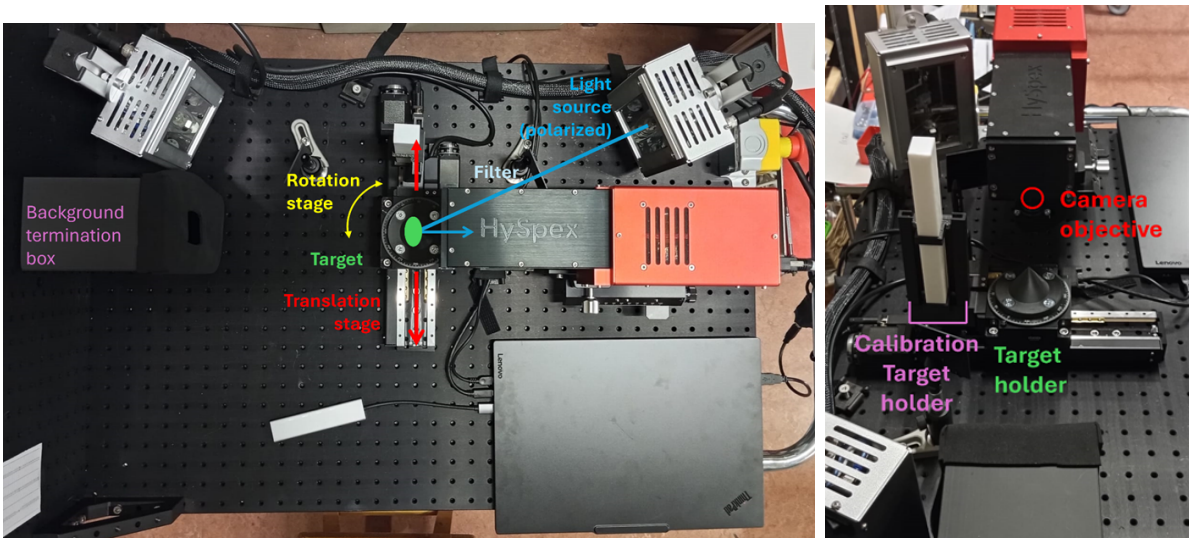

(a) (b)

Figure 8: a) Top view of the scanning setup. Light path through the system is depicted symbolically. b) Front view of the scanning setup. The calibration target is positioned at the same distance and within the same field of view as the sample to ensure optimal calibration.

3.3 Data Processing and Thresholding

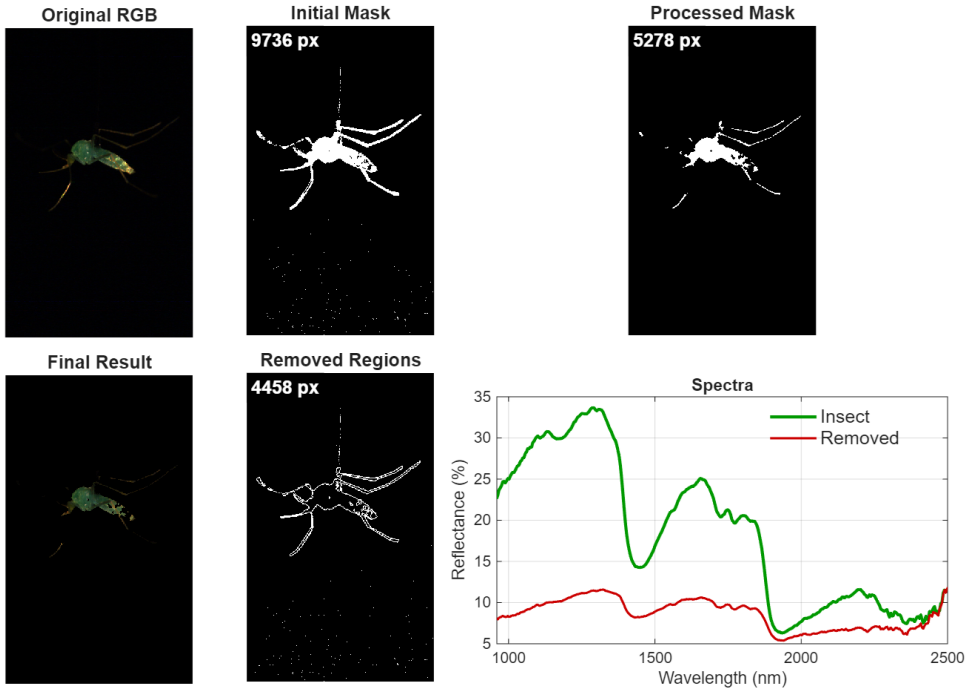

Figure 9: Example of the masking process applied to a de-polarized yaw-rotated scan of a female *Aedes aegypti*. The bands used for the false-color RGB images correspond to those used in existing entomological lidar systems, chosen for their relation to the water and melanin absorption bands.

After data acquisition, the hyperspectral files are radiance calibrated using Hyspex soft-

ware and converted into MATLAB files, and processed using Equation 6 to yield the final reflectance datacubes. The resulting reflectance files are then processed to extract only relevant pixels for analysis by applying a threshold mask and simple image processing. The masking is performed through a combination of intensity thresholding (sum of all bands), erosion-dilation, and object size thresholding. First, the lower and upper boundaries of intensities are set as median+2*IQR and 99.9 percentile respectively. The resulting binary mask is then eroded by 2 pixels and dilated by 1 to remove possible remnants of background and legs of the insect. Finally, all disconnected areas of size smaller than 30 pixels are rejected to further ensure a consistent contribution of insect legs to the signal. An example of the resulting masking process is shown in Figure 9.

3.4 Scan Geometry

The four-parameter diffuse reflectance model ($D_{1/2}$, α, l_{H_2O}, l_{mel}) was previously fitted by Li et al. [13] to a single observation angle per specimen. The experimental contribution of this thesis is to extend that characterization across viewing angles, by fitting the same four parameters throughout a rotational scan to resolve the angular dependence of each parameter in two orthogonal anatomical planes. We scanned 6 female *Aedes aegypti* mosquitoes, 3 pinned on the thorax (meaning rotation by yaw angle, see Figure 3) and 3 pinned on the end of the abdomen (rotation by roll angle). These two rotation axes were chosen because they lie in mutually orthogonal anatomical planes (sagittal and transverse). This allows the two 2D polar projections to span the angular information that a full 3D model would eventually require. We therefore have 2D projections of the optical parameters in two orthogonal planes.

3.5 Computational OCS Framework

A MATLAB framework was implemented to assemble per-frame parameters from hyperspectral scans of fresh insect bodies into a directional model. The framework draws on the spherical-harmonic description of [15] and takes spherical-harmonic coefficients as input for both body geometry and each of the four optical parameters, returning the backscatter optical cross-section (σ_{BS}) as a function of pitch, yaw, and wavelength. For example, if only the $Y(0,0)$ element is defined, the parameter will be modeled as a sphere of radius equal to the specified coefficient. For a simple case, such as a small mosquito where most of the light penetrates the entire body and escape from the other side, the optical properties are largely independent of the viewing angle since the body volume is almost uniformly illuminated. Here, a single coefficient for the $Y(0,0)$ harmonic is sufficient, as it models the parameter as a sphere with a radius equal to the input coefficient. The value of the parameter is therefore the same for every viewing angle.

For a larger and more anatomically detailed target such as a bumblebee, the backscattered signal can be highly sensitive to the viewing angle. For example, it may have a higher concentration of melanin (l_{mel}) on its anterior compared to its posterior, or different properties on its furry ventral side with many legs compared to the dorsal side. To describe such features, a simple $Y(0,0)$ model is not enough, and additional higher-order harmonic coefficients are required to capture this anisotropic reflectance. The reflectance parameters can therefore describe a more detailed directionality of insect anatomy, like higher concentration of melanin in the head etc. The parameter models undergo the same rotations as the physical body model, so that each viewing angle yields the corresponding

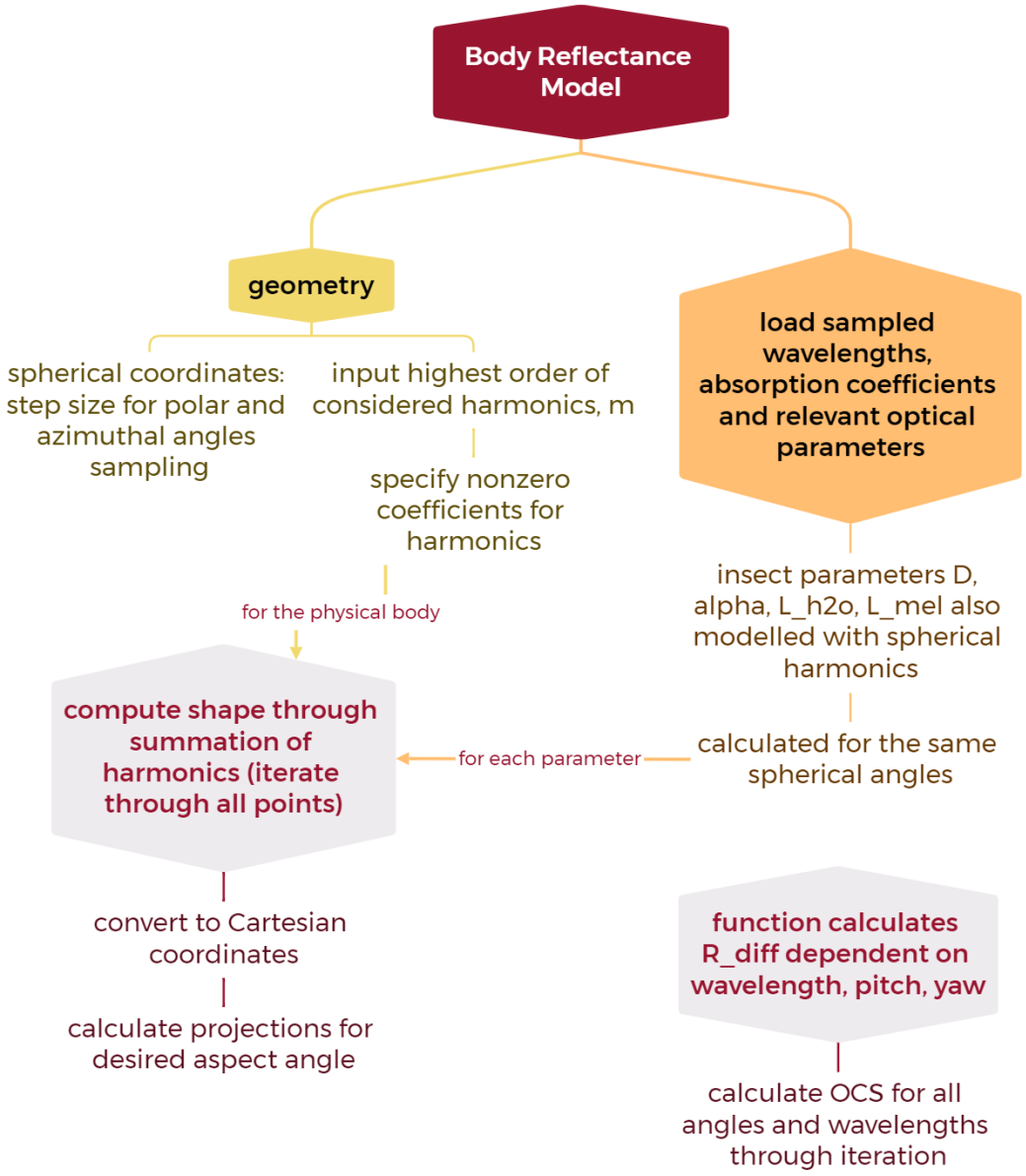

Figure 10: Conceptual flowchart of the model.

signal. The demonstration here uses mosquito data, but the script accepts higher-order inputs for a wide variety of insects.

Once the geometric and parameter models are defined, σ_{BS} is computed. The framework is adaptable; it can load either the previous published near-infrared dataset [13] or the newly acquired SWIR dataset, provided the input wavelength array is adjusted accordingly. In the demonstration shown here, the wavelength range and their corresponding absorption coefficients are loaded from previous data ([13]). The script iterates over all specified viewing angles (pitch and yaw) and wavelengths, as shown in Figure 10. For each unique combination, the projected area (A_p) is derived from the geometric model, and the diffuse reflectance (R_{diff}) is calculated from the four body-parameter models. The σ_{BS} is then simply the product of these two results ($\sigma = A_p \cdot R_{diff}$, eq 5). While this comprehensive process is run to demonstrate and visualize the full capabilities of the model, in practice, comparing to a single real measurement would only require running the calculation for that specific viewing angle and wavelength. The framework accepts

wavelength arrays and absorber spectra appropriate to either the near-infrared or SWIR range, so that it can be applied to existing datasets as well as the data acquired in this thesis.

4 Results and Discussion

4.1 Extraction of Optical Parameters

Examples of the model fit for a specimen across the two different rotational axes (yaw and roll) are shown in Figure 11. Although the camera's spectral range extends to 2500 nm, the signal becomes very noisy past 2100 nm. The analysis described below was performed in the restricted spectral range of 960-2100 nm for clarity. Using the masking procedure described in Section 3.3 (Figure 9), the mounting pin was successfully removed and saturated pixels were rejected, while most of the insect body and key features were preserved. The model of reflectance described in Section 2.3 is plotted against the recorded spectra for both yaw- and roll-rotated batches. As evidenced by the adjusted R^2 value shown in Figure 11, over 98% of the spectrum is explained by the model. The main discrepancy lies in the second water absorption band around 1930 nm, consistent with the two water bands sampling different effective volumes that a single l_{H_2O} cannot capture, as anticipated in Section 3.2.

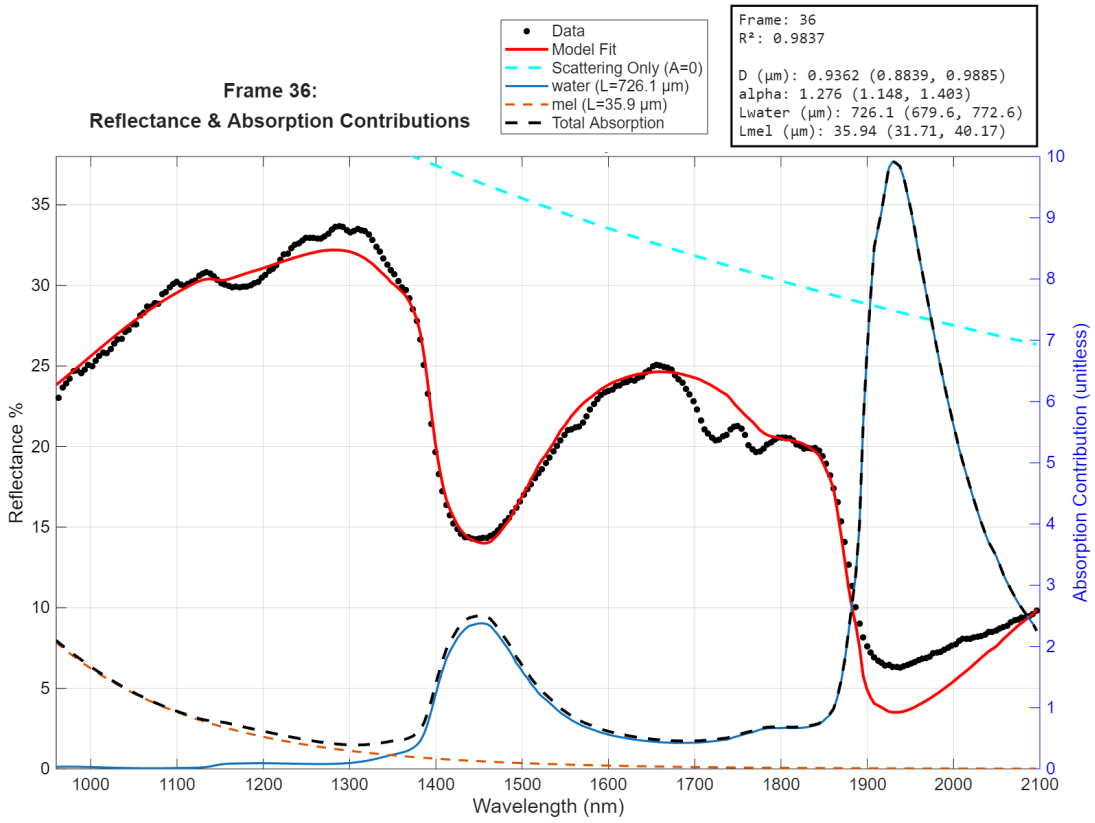

Figure 11: Decomposition of the reflectance model fit to a de-polarized yaw-rotated scan of a female *Aedes aegypti*. Black dots are the measured spectrum, the red curve is the full model fit, and the dashed cyan curve shows the pure scattering contribution in the absence of any absorbers. The blue and orange solid curves show the individual absorption contributions of water and melanin respectively, with their sum shown as the dashed black curve (right axis). Fitted values of $D_{1/2}$, α, l_{H_2O}, and l_{mel} together with the adjusted R^2 are listed in the inset.

4.2 Angular Dependence of Optical Parameters

The fitted optical parameters show clear angular dependence across both yaw and roll rotations (Figures 12 and 13). As expected, the projected area is largest when the mosquito is viewed from the sides and smallest from the front and back, producing the characteristic two-lobed pattern of an elongated body. The scattering parameter $D_{1/2}$follows the same angular dependence as the projected area in yaw, peaking from the sides and dropping at the front and back. The scattering exponent α is essentially isotropic across both rotation planes, although its absolute value varies between specimens, indicating that α captures a near-uniform property of the cuticle whose magnitude differs between individuals.

The effective melanin path length is largest from the front of the insect in yaw (Figure 12), consistent with the head being the most melanized region. *Aedes aegypti* also carries distinctive dark stripes along its dorsal abdomen, but these are interlaced with bright white scales whose internal scattering mean-free-path approaches the wavelength of light [13], raising the local scattering coefficient and reducing the contribution of melanin absorption to the spatially averaged spectrum. In roll (Figure 13) the melanin path length is more isotropic, although one specimen shows an increase near 90° rotation corresponding to the dorsal view.

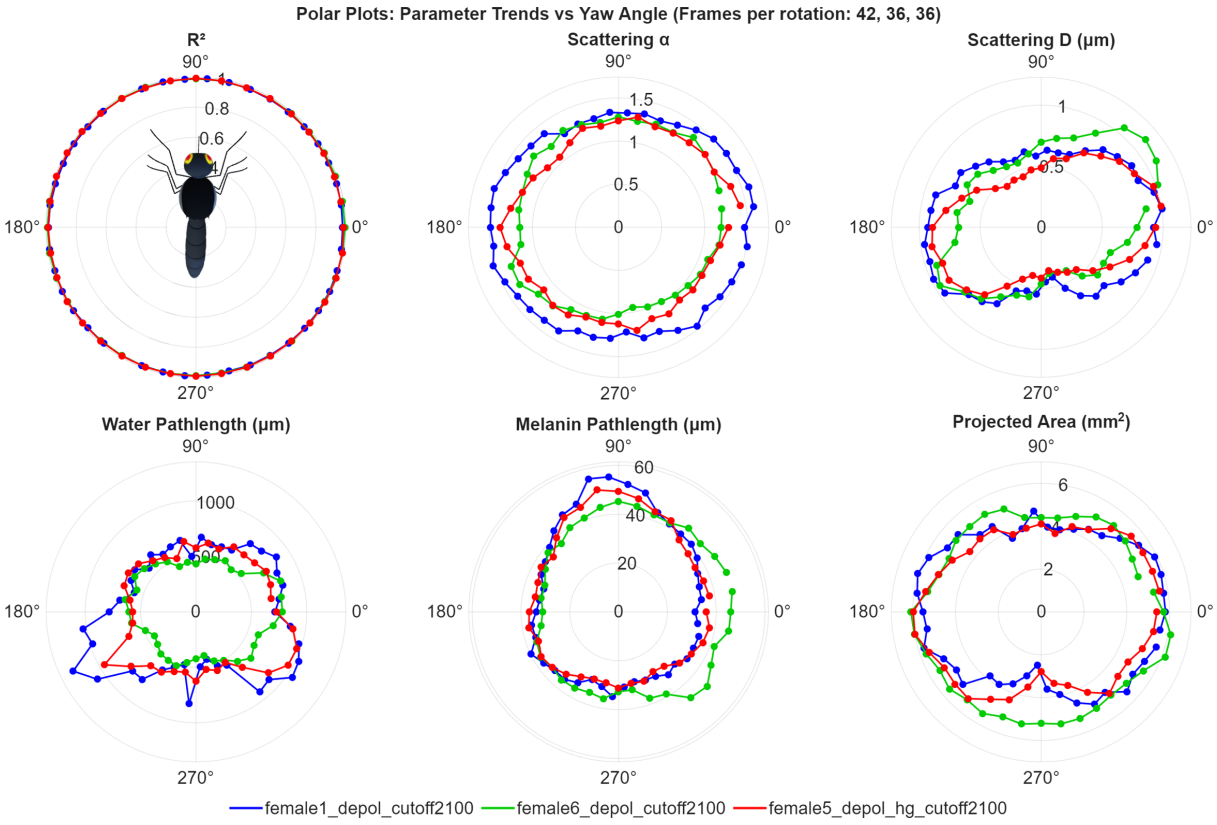

Figure 12: Yaw dependence of optical parameters from three female *Aedes aegypti* specimens. Each colored line corresponds to one individual. The cartoon mosquito silhouette in the R^2 panel indicates sample orientation; 0° corresponds to the side view. The scan of specimen 1 contains 42 angular samples instead of 36 due to a software configuration change.

The water path length behaves differently between the two rotation planes. In yaw, it is largest from the sides of the insect, with inter-individual variance exceeding 50% at

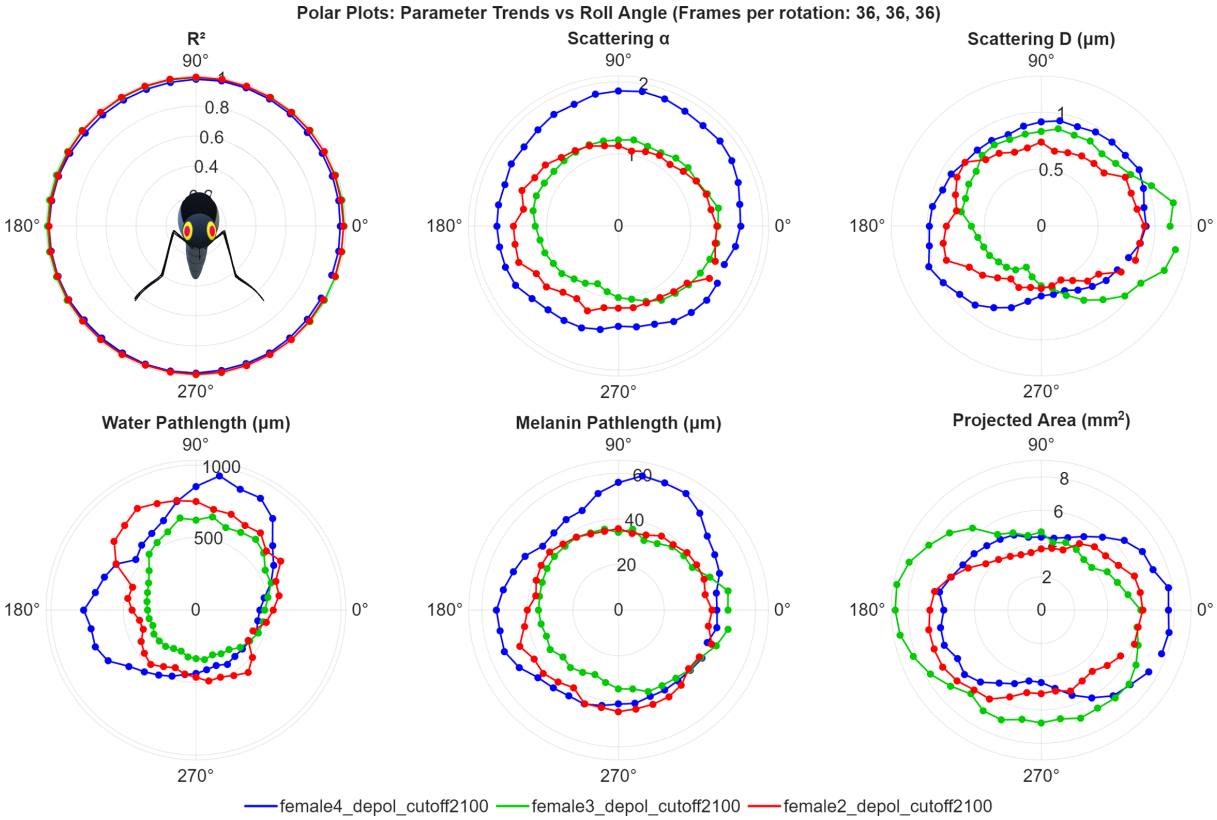

Figure 13: Roll dependence of optical parameters from three female *Aedes aegypti* specimens. Each colored line corresponds to one individual. Apparent misalignment between specimens reflects that the first frame of each scan was not acquired from exactly the same starting orientation and was adjusted during processing.

some angles. In roll, it shows a clear increase at the back of the insect. The latter trend may reflect a slight forward tilt of the specimen due to gravity when mounted at the tip of the abdomen, in which case the water path length lobe is shifted, implying that the true water path length is shorter from the sides than from the ventral or dorsal direction, consistent with a body cross-section that is narrower left-to-right than ventral-to-dorsal. Compared to the side-view values reported in [13], the fitted $D_{1/2}$ and l_{mel} are on average larger, l_{H_2O} is significantly larger, and α is smaller in this dataset. The larger l_{H_2O}in particular is consistent with the fit being pulled by the strong 1930 nm water band added by the extended SWIR range, which was not present in [13]. Specimen age and recent feeding on the sugar water provided in their enclosure may also contribute to the observed differences.

The fitting was performed with the MATLAB curve fitting toolbox; 95% confidence intervals on the calculated parameters are narrow relative to the inter-specimen variance. Roll scans produced more consistent angular profiles between individuals than yaw scans, reflecting the differences in mounting geometry discussed in Section 4.3. Mean profiles across the three specimens per rotation plane are shown in Supplementary Figures S1 and S2, though with only three specimens per rotation the mean is indicative rather than statistically robust, and a larger campaign is needed to consolidate the angular trends reported here.

4.3 Methodological Challenges and Limitations

The polar trends in Section 4.2 show what the model picks up, but they also raise the question of how much of the variation is biological and how much comes from the measurement itself.

4.3.1 Insect and Scan Geometry

Insect bodies are bilaterally symmetric in principle, but the mounting process, particularly the placement of the pin and the post-mortem posture of the specimen frequently breaks this symmetry in our setup. Mosquitoes pose a particular challenge to describe geometrically due to their small size and comparatively long, thin limbs. The thickest part of the body is the thorax (around 500 µm), followed by the abdomen (around 400 µm) and the head (around 300 µm)[25]. In diagrams (and live specimen), these largest parts form an approximately ellipsoid shape with bilateral symmetry (see Figure 14). Freshly killed ones, however, may have their abdomen "curled" underneath or to the sides, therefore becoming a more irregular shape. This makes mounting the pin precisely in anatomical planes very difficult and negatively effects the reproducibility of analysis results. Moreover, the center of gravity need not coincide with the anatomical planes, which is particularly problematic when mounting specimen for roll rotation, since the insect will likely lean forward when mounted at the tip of the abdomen. This forward tilt could explain the shift of the water path length lobe seen in the roll-rotated batch (Figure 13), and shows how a small geometric error can show up as a misleading directional trend in the fitted parameters.
Furthermore, we must consider how the size of the target relates to the depth of field of the imaging system. In our case, the female *Aedes aegypti* mosquitoes have approximate body length of mere 5mm, yet it was still impossible to have both the front and back of the specimen in focus during yaw rotation. We are using a microscope lens to distinguish as much detail as possible, but the depth of focus is limited. For larger targets, like a cricket or house fly, this problem is even more significant.

4.3.2 Image Processing and Masking

Masking decisions affect which pixels contribute to the averaged spectrum and therefore the fitted parameters. The procedure has to reject background and mounting pin while preserving the body, but deciding what counts as 'body' is non-trivial. It is worth noting that deciding which parts of the insect are relevant is a troublesome question in itself. In real lidar observations, we will never see an insect with its legs removed, but in ex-vivo measurements they are a source of strong variation to the signal which is inconsistent and inevitable. When illuminated with intense light (as is required for hyperspectral imaging), these features may scatter and reflect light in a way that makes the intensity ranges of legs and body pixels overlap, therefore making it difficult to separate the two through thresholding. On the other hand, the erosion-dilation process, which is essential for removing the scattering contribution of the mounting pin, will inevitably also remove large portions of the thin legs.

Since the spectra used in parameter fitting are averaged over all selected pixels, inconsistencies in masking can have a significant impact on the deduced parameter values. For example, we can expect the legs of the mosquito to have less water than the body due to the difference in their ratio of surface area to volume - the thin legs will evaporate water much faster than the body. If we then have a mask that does not completely reject pixels

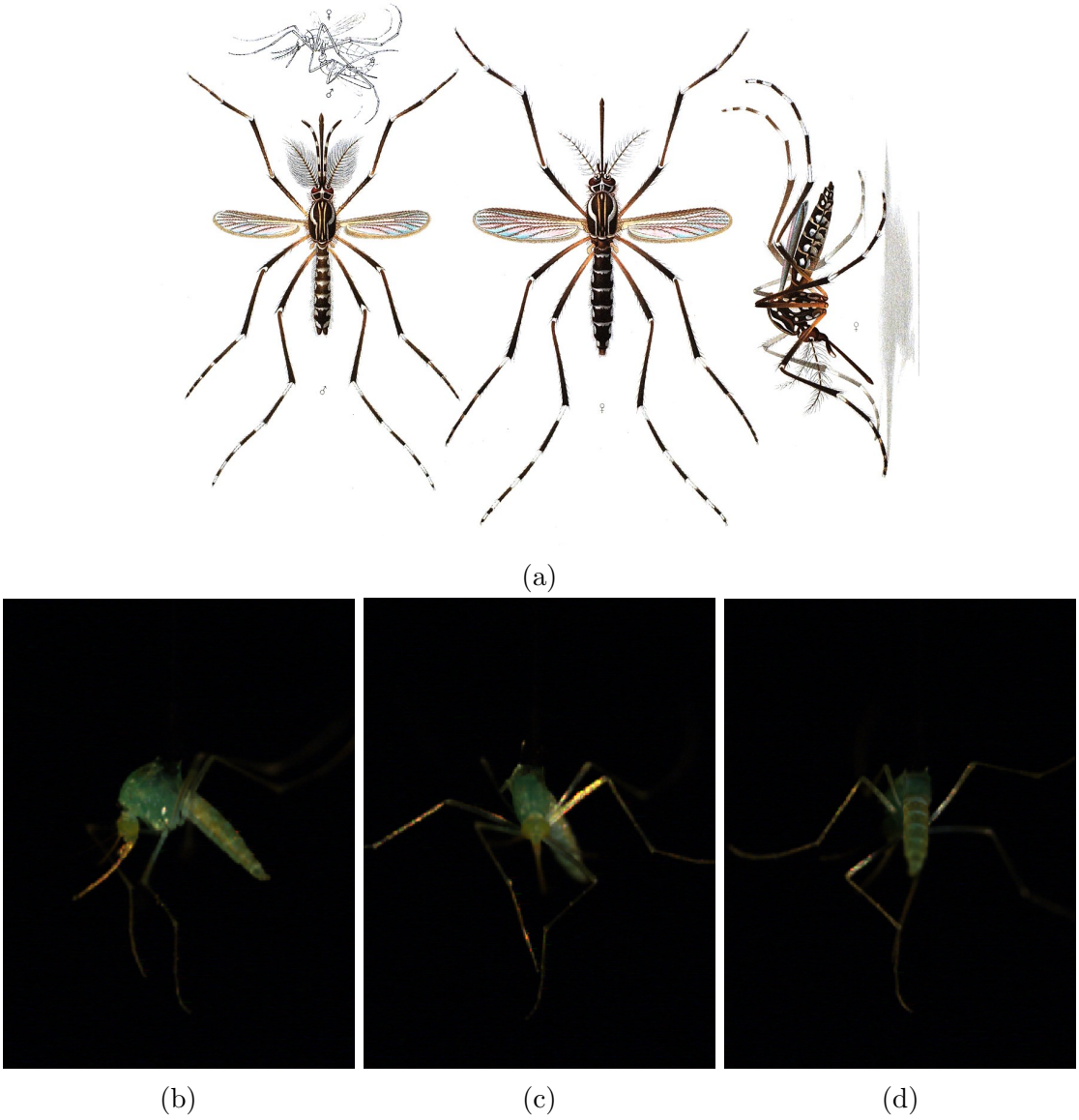

(a)

(b) (c) (d)

Figure 14: Comparison of (a) *Aedes aegypti* anatomical illustration [26] and (b, c, d) false color de-polarized images of specimen female6 curving laterally, seen from the side, front, and back. In (a), the leftmost image shows a male individual, while the middle and right ones show a female.

from the legs, we may end up with some frames with a 95% to 5% ratio of body pixels to leg pixels and some with a ratio of 70% to 30%. Since the proportion of pixels from the thin legs is changing, the averaged spectra will be affected and less water absorption will appear in the frames with more leg signal.

4.3.3 Environmental and Biological Variances

The measurements reported in this thesis were taken exclusively on female *Aedes aegypti*. This was driven primarily by availability: the live specimens provided contained far more females than males, and the males that were available were considerably smaller (under 2 mm in total length in many cases) and posed a challenge to handle and mount. Male mosquitoes also carry plumose ("fuzzy") antennae, which would be expected to alter the

scattering signature noticeably compared to the smooth filaments of females. The sex dependence of the optical parameters is therefore not captured in the present dataset and is an obvious gap for future work.

In addition, all specimens used in this study were fed exclusively on sugar water, which is not a fully realistic representation of what a field lidar would encounter. Blood-fed females in particular carry hemoglobin signatures and substantially elevated water content, and characterising the feeding-state dependence of the fitted parameters is outside the scope of this work but would be especially relevant for vector surveillance applications.

A further concern is that each scan consists of 36 frames acquired sequentially during a full rotation. With a small specimen exposed to a warm tungsten lamp throughout the scan, the water content of the body very plausibly decreases over the course of the acquisition. This means that the angular trends in water path length reported in Section 4.2 (Figures 12 and 13) are at risk of containing a time-dependent desiccation component that has been mistakenly attributed to viewing angle, since angle and time are confounded in our scanning protocol. A simple future test would be to scan the same specimen repeatedly from a fixed orientation at increasing time delays, allowing the rate of water loss under the lamp to be quantified and the angular signal to be corrected accordingly.

Finally, the SWIR light used in our measurements can penetrate the small volume of a mosquito body, meaning that internal structures contribute to the recorded reflectance. Specimens in this study were mounted using UV-curing adhesive, and if any glue residue remained inside or on the body of the mosquito and was not fully rejected by the masking procedure, its spectral signature could contaminate the fitted parameters. The magnitude of this effect was not quantified in the present work and would warrant a controlled measurement of a glue sample under the same illumination conditions.

4.4 Application of the Simulation Framework

The simulation framework presented here serves as a proof-of-concept for integrating multidirectional spectral data. For this demonstration, the framework was run on the previously published near-infrared dataset from [13] with $Y_{0,0}$ placeholders for the angular terms, in order to isolate and verify its computational behavior. Expanding the SWIR polar trends from Section 4.2 into spherical harmonic coefficients could not be completed within the time frame of this thesis; once this step is carried out in future work, the resulting coefficients can be directly integrated into the established pipeline.

The model simulates a 3D insect body-shape from input spherical-harmonic coefficients, with no upper limit on how many harmonics are used (see the rendering in Figure 15a). The same complexity is allowed for each scattering parameter (Figure 15), enabling directional dependence of reflectance. The model can be rotated by any combination of pitch and yaw angles and returns the corresponding altered projection area. For each orientation, the backscatter σ_{BS} value for all wavelengths is calculated.

The characteristic information of the insect is stored in a set of matrices describing the spherical harmonics coefficients for each relevant parameter. This way, a library can be built from just these coefficients and the 3D structure only needs to be rendered when needed. Altogether, this replicates the light scattering effect of an insect body and lays the foundation towards building a complete adaptable insect scattering model. Figure 16 shows the calculated σ_{BS} for selected example viewing angles. The spectral shape comes from the diffuse reflectance model, while the angular shape comes from the projected area.

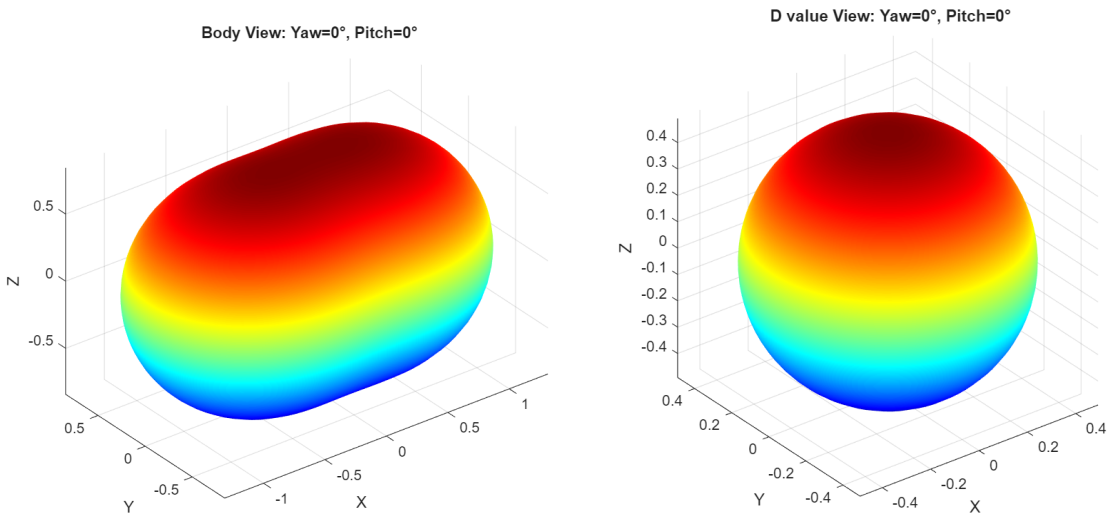

(a) (b)

Figure 15: a) Rendering of the 3D insect body-shape simulated with spherical harmonics. For the simple "cigar" shaped body we take $Y(0,0) + 0.5Y(2,0)$. We imagine the source/detector in the YZ plane, so looking "head-on" the body would appear as a circle. b) Rendering of the 3D "parameter sphere" for $D_{1/2}$. In this case, we only use the fundamental $Y(0,0)$, but the model could be fitted to real life measurements to create a more detailed representation.

So far, the model was only tested on co-polarized backscattered light, assuming only water and melanin absorption in the insect. For a mosquito, this is sufficient, but other insects might require the inclusion of chitin or lipids as well. This could be resolved easily though, by extending the reflectance function with additional terms.

4.5 From Laboratory Specimens to Field Lidar Observation

In this thesis we scanned six female *Aedes aegypti* mosquitoes, three pinned on the thorax for yaw rotation and three pinned on the abdomen for roll rotation. The choice of species was driven by two main factors. First, live specimens were available through collaboration with SLU, who breed and study this mosquito; *Aedes aegypti* is a globally important disease vector and a popular subject of entomological study, although it is not naturally widespread in Sweden. Second, we wanted to be able to compare against and extend the characterization reported in [13], where the same diffuse reflectance model was applied over a narrower near-infrared range. Extending the spectral window to the SWIR adds a second strong water absorption band, allowing us to test how well the model performs over a wider range and providing a useful check on the fitted parameters.

This thesis work is essentially a test and an initial step: seeing how well freshly killed specimens can be mounted, how reliably their body features can be captured from two main anatomical planes, and how this data can be exported into a 3D model from which lidar signals can later be simulated as a function of observation angle and wavelength. Field deployment looks very different. In Sweden, a freshly killed, pinned, dewinged, sugar-fed *Aedes aegypti* under controlled tungsten illumination is not what a deployed lidar would ever observe. The purpose of starting in a well-controlled environment is, as motivated in the Aim and Scope, to isolate the body component first, an approach toward giving lidar a better clue of what kind of insect is being observed, without having

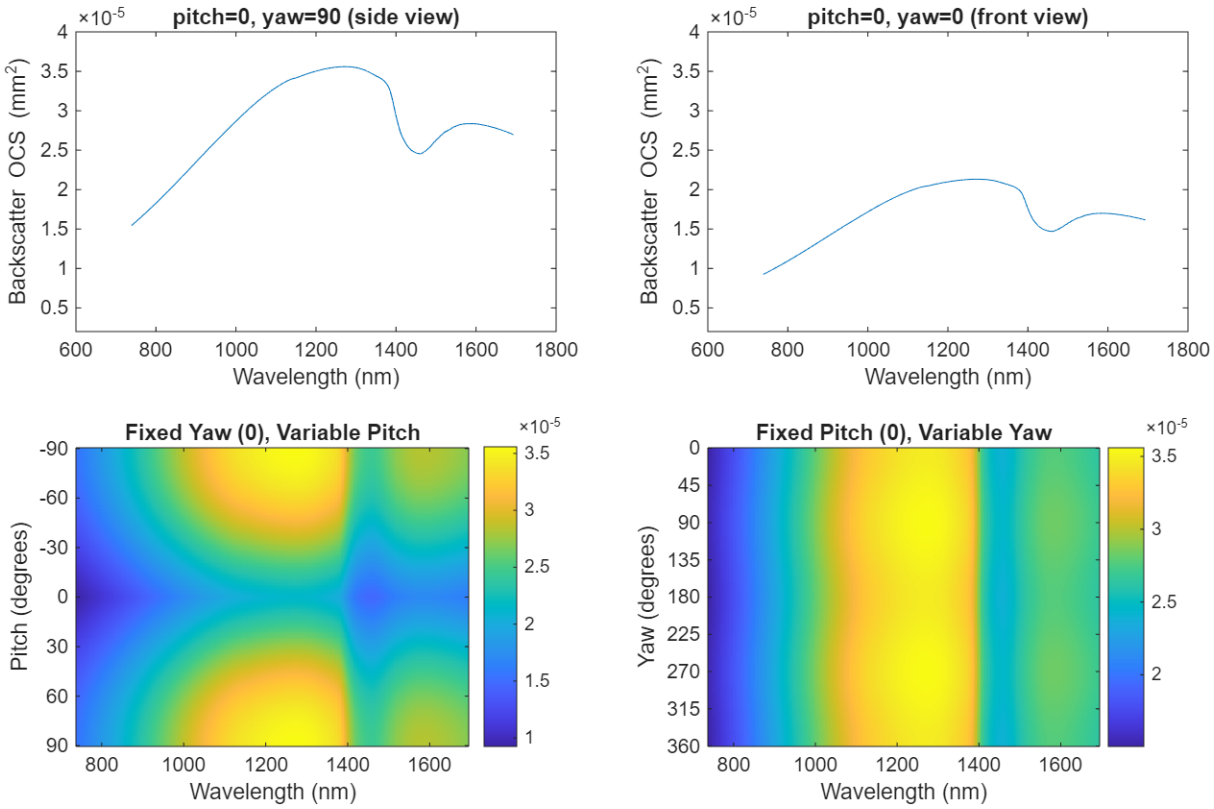

Figure 16: Visualization of the model output. On the top left, we see the wavelength dependent σ_{BS} when looking at the insect from the side. On the top right, we have the corresponding plot when looking at the insect head-on, giving smaller σ_{BS} values due to the decreased projection area from that perspective. On the bottom left is a heatmap showing the wavelength dependent σ_{BS} for all pitch angles if the yaw was kept at 0, and on the bottom right a similar figure where the pitch is kept at 0 instead. Since we kept the optical parameters uniform across the body, the response is only defined by the spectral pattern and the changing projection area of the body. We can see in both bottom figures the sharp drop corresponding to the water absorption seen in the top figures.

to physically release millions of species to build empirical training data. Within this framing, mosquito is a sensible starting species: it has a high wingbeat frequency, an elongated body shape that is well-suited to low-order spherical harmonic approximation, and an extensive existing literature base. Later, when the modelling effort expands into the wing component and the full signal-band simulation including wing dynamics [27], having this body-only reference in hand will be a useful starting point.

5 Conclusions

In this thesis, an adaptable MATLAB model of insect scattering has been developed based on physical principles of light interaction with biological matter. The model calculates the backscatter σ_{BS} for de-polarized light for the insect body, accommodating spectral reflectance, as well as full pitch and yaw dependence of the projected area and user-defined insect parameters. The framework was verified end-to-end on the previously published near-infrared dataset from Li et al. [13], confirming its computational behaviour before application to new data.

New hyperspectral data of *Aedes aegypti* females was collected in the extended SWIR range (960–2100 nm) to characterize the optical parameters of the body and their angular dependence. Decomposing these angular profiles into spherical harmonic coefficients for direct ingestion by the framework was outside the time scope of this thesis, but the pipeline is in place for this step to be carried out in future work. Scans in full yaw and roll rotations were performed for both co- and de-polarized backscatter configurations in broad SWIR range. De-polarized images were then processed to extract averaged spectra from each frame of the scans. Optical parameters describing scatterance and effective path lengths of water and melanin were obtained through curve fitting of the individual spectra using a diffuse reflectance model. Analysis of the data from the fresh insects revealed higher values of the investigated parameters than reported in previous study. The number of specimens processed in this thesis is not sufficient to perform robust statistical analysis and definitively characterize the species.

6 Outlook

This thesis establishes a foundation for a physics-based model to simulate insect scattering signatures, providing an alternative to the impractical task of building empirical databases through physical specimen collection. With the body component characterized, several research directions are accessible. Firstly, co-polarized data collected for this thesis project can be analyzed to reveal information on specular reflections, which could tell us more about surface structure of the mosquito bodies. Evidently, bigger sample size is needed in future work, 3 specimen per orientation is the most that could have been achieved as part of this thesis but it hardly facilitates robust statistics. When similar studies are done in the future, the specimen could be weighed before and after scanning, as well as after complete desiccation to further inform on body mass and water content, either validating or disproving the water path lengths resulting from spectral analysis. Further investigation is also needed to determine why the second water absorption band differs from the predictions of the current reflectance model. Furthermore, the next scanning campaign could involve removing the legs of the studied insects, thereby simplifying image processing and improving the veracity of spectral analysis. When compared with measurements taken with legs remaining, the strength of influence of limb presence could be estimated, possibly aiding future modeling attempts. Male specimen also need to be studied to compare differences between sexes. Notably, male mosquitos have fluffy antennae (see leftmost image of subfigure 14a), which could affect light scattering, while recently fed females would have contributions from ingested blood.

When applied to other insects, the model might present new challenges and aspects of reflectance that were previously not considered. For example, preliminary analysis of cricket hyperspectral images (presented in Figure 17) has revealed significant absorption contributions from lipids that were not present in the mosquito spectra. When a similar measurement was taken of a fresh blue bottle fly, which is black and highly melanized, the spectral contributions from melanin absorption were so strong that it became impossible to resolve the scatterance contributions. This is likely due to the current diffuse reflectance model being designed for thin, poorly scattering targets [20]. Other reflectance models from [20] could be tested for highly melanized insects, as the paper contains another section for reflectance from dark targets. Additionally, bigger targets like crickets or flies scatter light differently and face more significant problems due to depth of focus limitations as seen in Figure 20. Combining the body model presented here with wing interference signatures previously studied in the group [24], using the same camera and wavelength range, would be a natural next step toward synthesizing full lidar waveforms.

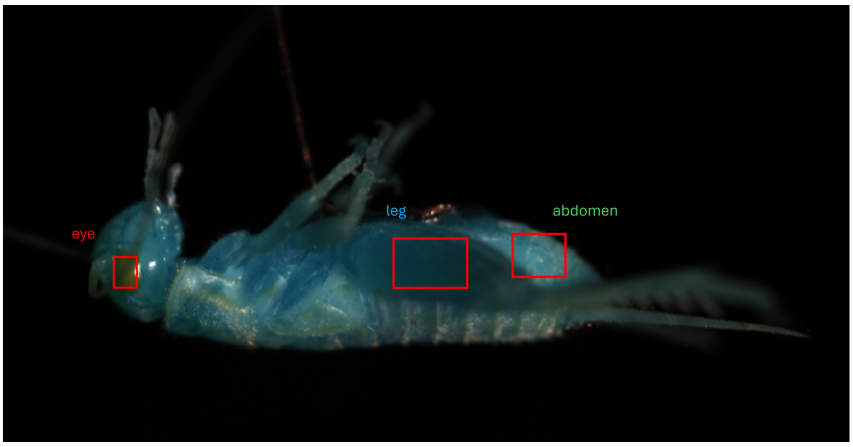

(a)

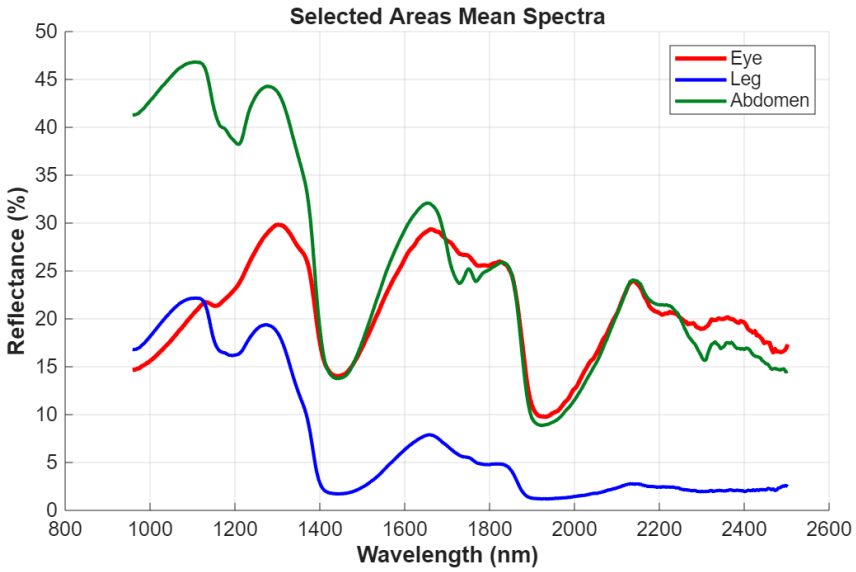

(b)

Figure 17: Qualitative comparison of spectra extracted from different regions of a cricket's body. The signal from the eye shows stronger melanin absorption, consistent with the eye being a highly melanized organ. All regions present high water absorption, as expected of fresh specimen. Notably, the abdomen signal contains contributions from lipids (triglycerides) around 1200 nm and 1750 nm. Crickets do store fat in their abdomen, explaining the lipid content showing only in that region of the body.

(a) Co-polarized (b) de-polarized

Figure 18: False color images of blue bottle fly *Calliphora vomitoria*

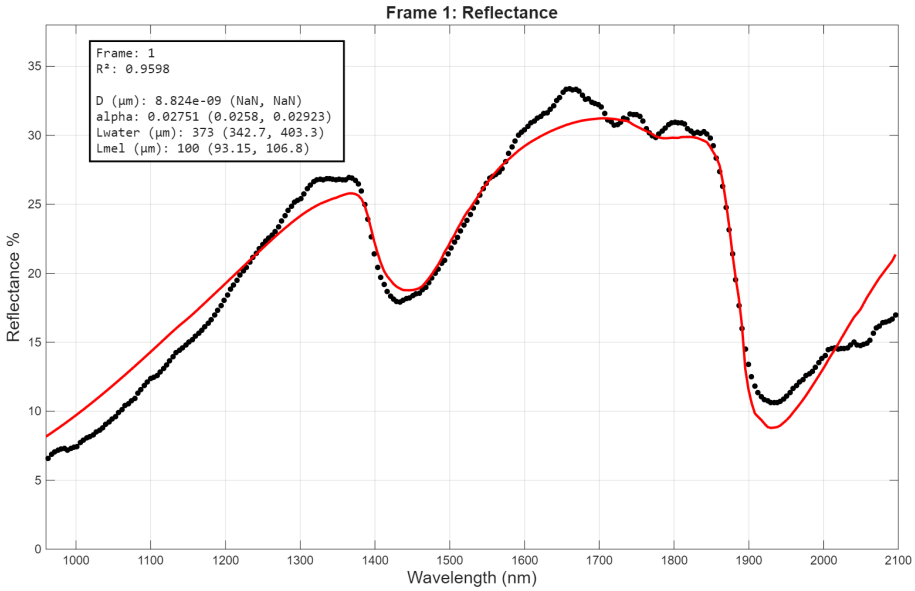

Figure 19: Example of spectral fitting for fly specimen presented in Figure 18.

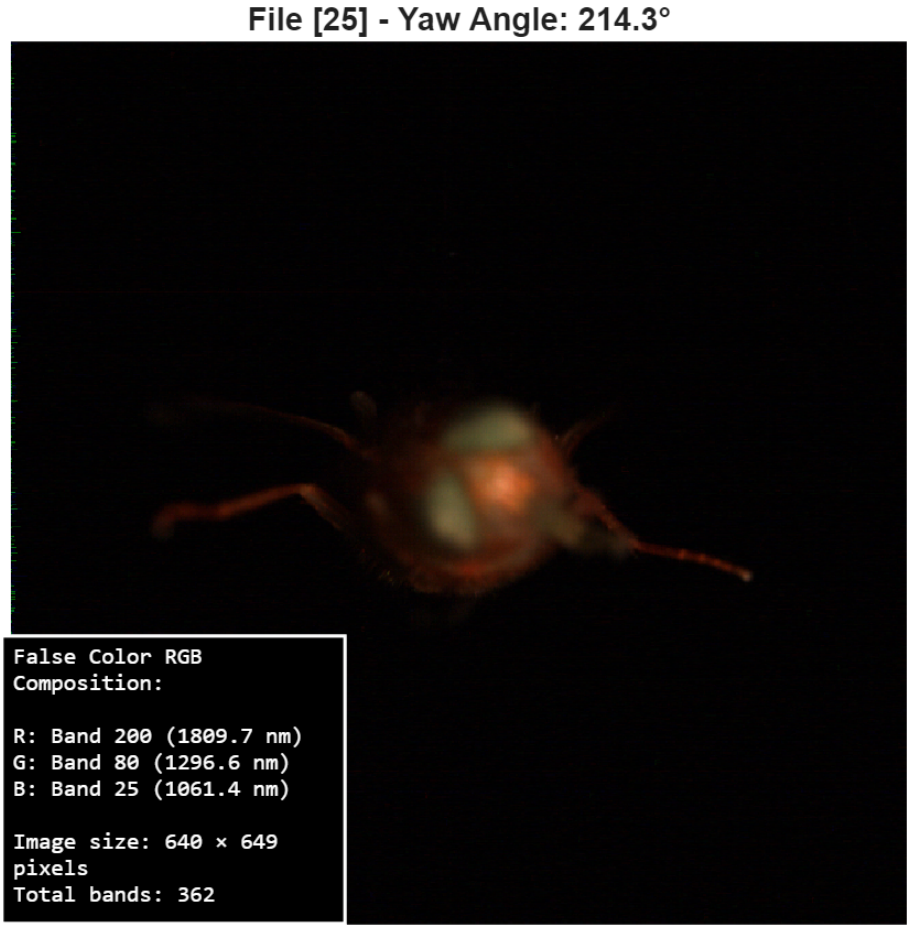

Figure 20: False color of the fly seen from the front. Since the camera was focused at the side-view sample position and the specimen was mounted in the middle of the abdomen, the rotation shifted the surface of the specimen out of the focus plane of the camera.

References

[1] Sanhita Chowdhury et al. "Insects as bioindicator: A hidden gem for environmental monitoring". In: *Frontiers in Environmental Science* 11.11 (Mar. 2023). DOI: https://doi.org/10.3389/fenvs.2023.1146052.

[2] R. W. Sutherst. "Global Change and Human Vulnerability to Vector-Borne Diseases". In: *Clinical Microbiology Reviews* 17.1 (Jan. 2004), pp. 136–173. DOI: https://doi.org/10.1128/cmr.17.1.136-173.2004.

[3] Dave Karlsson et al. "The Swedish Malaise Trap Project: A 15 Year Retrospective on a Countrywide Insect Inventory". In: *Biodiversity Data Journal* 8 (Jan. 2020). DOI: https://doi.org/10.3897/bdj.8.e47255.

[4] Barna Páll-Gergely et al. "Identification crisis: a fauna-wide estimate of biodiversity expertise shows massive decline in a Central European country". In: *Biodiversity and Conservation* 33.13 (Nov. 2024), pp. 3871–3903. DOI: https://doi.org/10.1007/s10531-024-02934-6.

[5] Meng Li, Hampus Månefjord, and Mikkel Brydegaard. "Resolving fast Wingbeat Flashes in situ with Entomological Lidar". In: *2024 IEEE Photonics Conference (IPC)* (Nov. 2024), pp. 1–2. DOI: https://doi.org/10.1109/ipc60965.2024.10799610.

[6] David Dreyer et al. "Robust and diverse multidimensional statistical moments in dual-band entomological lidar for improved real time insect monitoring". In: *Journal of Experimental Biology* (May 2026). DOI: https://doi.org/10.1242/jeb.251761.

[7] Hampus Månefjord et al. "Stratification of insect diversity and daily activity patterns in the West African virgin forest Taï assessed by entomological Lidar". In: *Scientific Reports* 15 (July 2025). DOI: 10.1038/s41598-025-05200-z. URL: https://www.nature.com/articles/s41598-025-05200-z (visited on 10/14/2025).

[8] Meng Li et al. "Potential for identification of wild night-flying moths by remote infrared microscopy". In: *Journal of The Royal Society Interface* 19.191 (June 2022). DOI: https://doi.org/10.1098/rsif.2022.0256.

[9] Hui Chen et al. "Lidar as a potential tool for monitoring migratory insects". In: *iScience* 27.5 (May 2024), p. 109588. DOI: https://doi.org/10.1016/j.isci.2024.109588.

[10] Klas Rydhmer et al. "Photonic sensors reflect variation in insect abundance and diversity across habitats". In: *Ecological indicators* 158 (Jan. 2024), pp. 111483–111483. DOI: 10.1016/j.ecolind.2023.111483.

[11] Song-Quan Ong et al. "InsectRoleVision: A computer vision system to study arthropod diversity and functional roles". In: *Ecological Informatics* (Apr. 2026), p. 103701. DOI: https://doi.org/10.1016/j.ecoinf.2026.103701.

[12] Nigel E. Stork. "How Many Species of Insects and Other Terrestrial Arthropods Are There on Earth?" In: *Annual Review of Entomology* 63.1 (Jan. 2018), pp. 31–45. DOI: https://doi.org/10.1146/annurev-ento-020117-043348. URL: https://pubmed.ncbi.nlm.nih.gov/28938083/.

[13] Meng Li et al. “Deadliest Animals with the Thinnest Wings: Near-Infrared Properties of Tropical Mosquitoes”. In: *Applied Spectroscopy* 79 (June 2025), pp. 1625–1639. DOI: 10.1177/00037028251341317.

[14] Meng Li et al. “Bark beetles as lidar targets and prospects of photonic surveillance”. In: *Journal of biophotonics* 14.4 (Dec. 2020). DOI: https://doi.org/10.1002/jbio.202000420.

[15] Mikkel Brydegaard. “Towards Quantitative Optical Cross Sections in Entomological Laser Radar – Potential of Temporal and Spherical Parameterizations for Identifying Atmospheric Fauna”. In: *PLOS ONE* 10 (Aug. 2015), e0135231–e0135231. DOI: 10.1371/journal.pone.0135231. (Visited on 09/25/2023).

[16] Ch Brechbühler, Guido Gerig, and Olaf Kübler. “Parametrization of Closed Surfaces for 3-D Shape Description”. In: *Computer Vision and Image Understanding* 61 (Mar. 1995), pp. 154–170. DOI: 10.1006/cviu.1995.1013. (Visited on 04/24/2023).

[17] L. Kou, D. Labrie, and P. Chylek. “Refractive indices of water and ice in the 0.65–2.5 μm spectral range.” In: *Appl. Opt.* 32 (1993), pp. 3531–3540.

[18] Darren Roblyer et al. “Review of shortwave infrared imaging and spectroscopy in tissue [Invited]”. In: *Biomedical Optics Express* 16.12 (Nov. 2025), p. 5028. DOI: https://doi.org/10.1364/boe.577163.

[19] V. Alistair Drake, Djordje Mirkovic, and Martin J. Steinbauer. “Insects as radar targets: size, form, density and permittivity”. In: *International Journal of Remote Sensing* 45.9 (Apr. 2024), pp. 2985–3002. DOI: https://doi.org/10.1080/01431161.2024.2339203.

[20] Paul Kubelka. “New Contributions to the Optics of Intensely Light-Scattering Materials Part I”. In: *Journal of the Optical Society of America* 38.5 (May 1948), p. 448. DOI: https://doi.org/10.1364/josa.38.000448.

[21] Tomas Svensson et al. “Near-infrared photon time-of-flight spectroscopy of turbid materials up to 1400 nm”. In: *Review of Scientific Instruments* 80 (June 2009), p. 063105. DOI: 10.1063/1.3156047.

[22] Johnson Andrew and Ananya Bar. “Morphology and morphometry of Aedes aegypti adult mosquito.” In: *Annual research & review in biology* 3.1 (Feb. 2013), pp. 52–69.

[23] N/A. Main specifications. 2026. URL: https://www.hyspex.com/hyspex-products/hyspex-classic/swir-640.

[24] Meng Li et al. “Discrimination of Hover Fly Species and Sexes by Wing Interference Signals”. In: *Advanced Science* 10.34 (2023), p. 2304657. DOI: https://doi.org/10.1002/advs.202304657. eprint: https://advanced.onlinelibrary.wiley.com/doi/pdf/10.1002/advs.202304657. URL: https://advanced.onlinelibrary.wiley.com/doi/abs/10.1002/advs.202304657.

[25] Jannat Amrin Luna et al. “Label-free visualization of internal organs and assessment of anatomical differences among adult Anopheles, Aedes, and Culex mosquito specimens using bidirectional optical coherence tomography”. In: *Optics & Laser Technology* 168 (Jan. 2024), p. 109849. DOI: https://doi.org/10.1016/j.optlastec.2023.109849.

[26] Emil August Göldi. *Os mosquitos no Pará. Reunião de quatro trabalhos sobre os mosquitos indigenas, principalmente as especies que molestam o homem. / Pelo professor Dr. Emilio Augusto Goeldi. Com 100 figuras no texto e 5 estampas chromolithographicas*. Provided by London School of Hygiene & Tropical Medicine Library & Archives Service. Digitized by the Internet Archive in 2015. Pará, Brazil: C. Wiegandt, 1905.

[27] Richard J. Bomphrey et al. "Smart wing rotation and trailing-edge vortices enable high frequency mosquito flight". In: *Nature* 544.7648 (Apr. 2017), pp. 92–95. DOI: https://doi.org/10.1038/nature21727. URL: https://www.nature.com/articles/nature21727?sf66762390=1.

7 Appendix. Supplementary Data

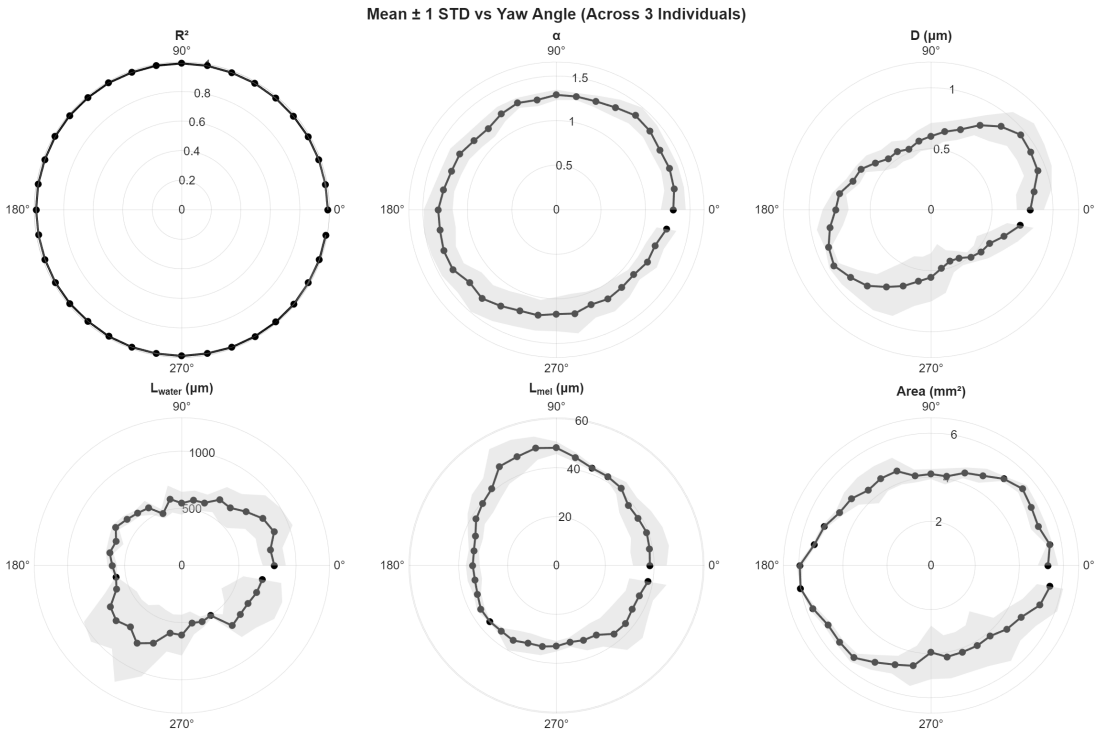

Figure S1: Mean values of fitted parameters for the yaw-rotated batch. Data from female 1 has been resampled onto 36 data points for the purpose of calculating the mean values.

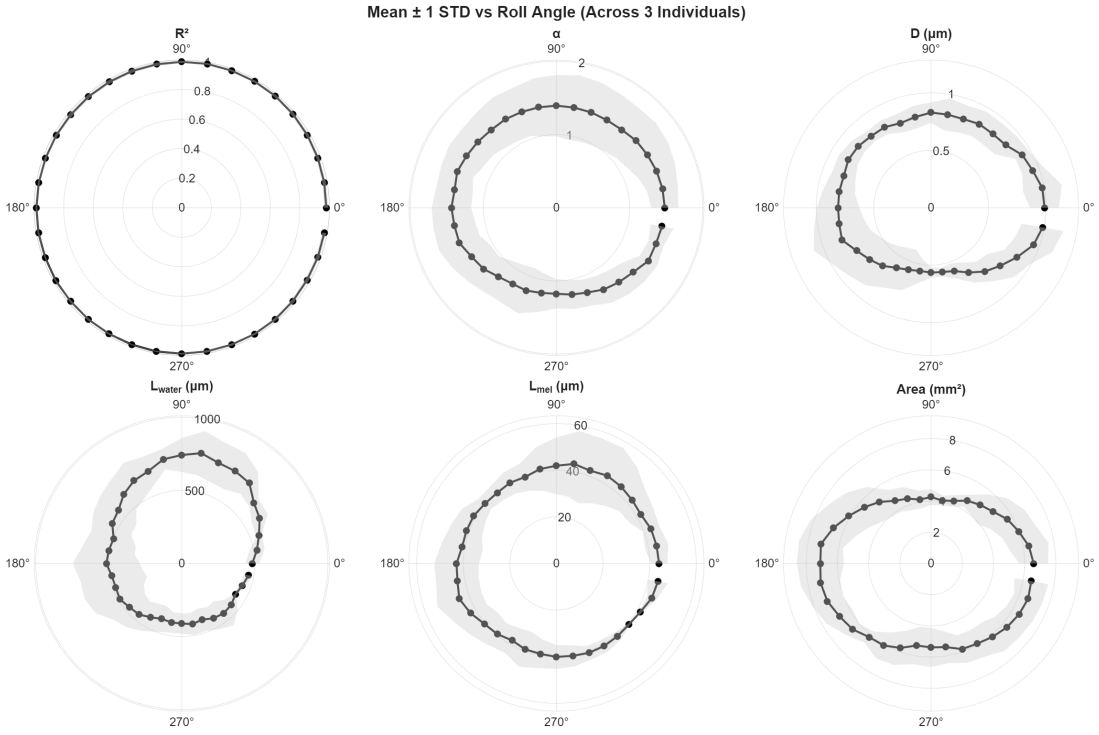

Figure S2: Mean values of fitted parameters for the roll-rotated batch.

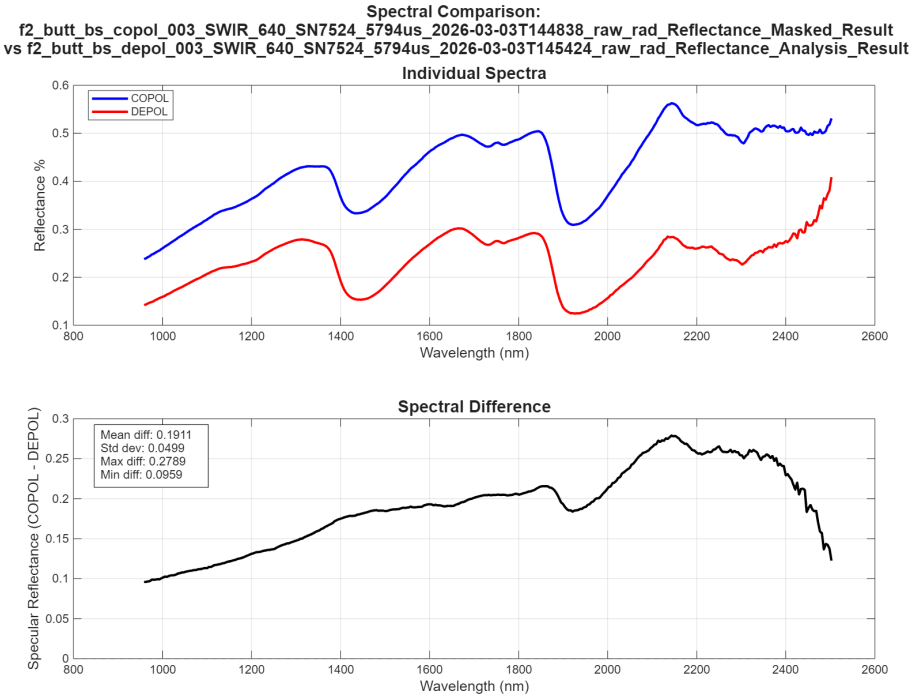

Figure S3: Specular reflectance in female2 (teflon correction was not applied)